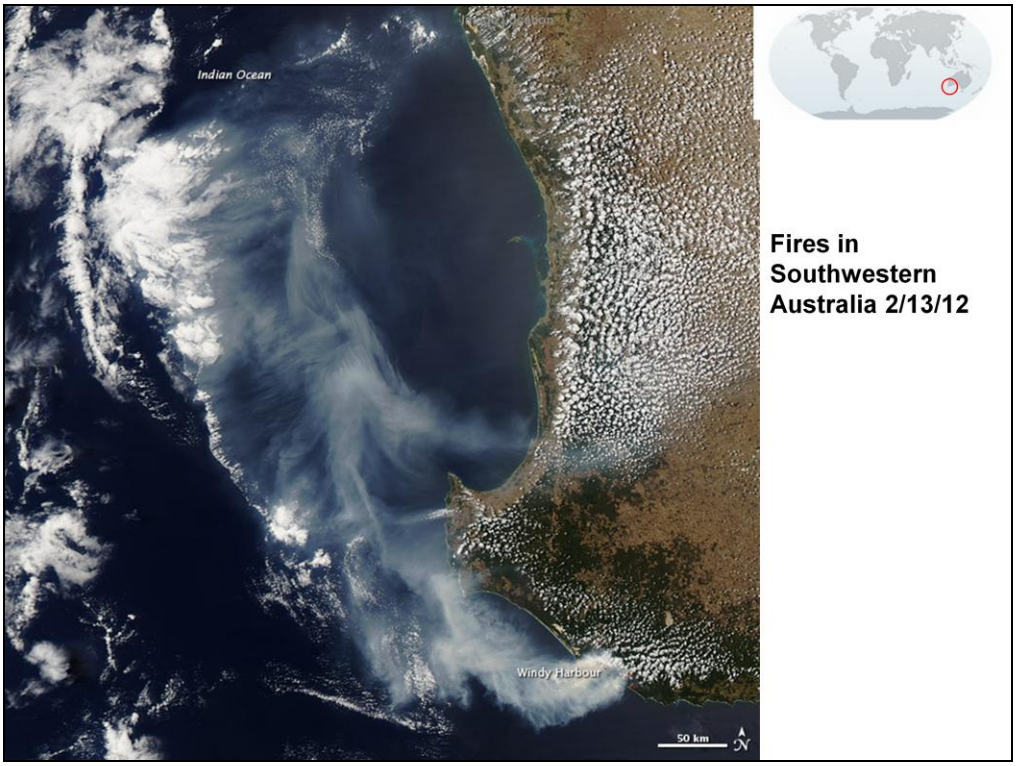

Fires in southwestern Australia sent a massive smoke plume over the Indian Ocean on February 13, 2012. The Moderate Resolution Imaging Spectroradiometer (MODIS) on NASA's Aqua satellite took this image the same day.

In this natural-color image, red dots show areas where MODIS detected unusually high surface temperatures associated with actively burning fires. The gray-beige smoke blows in a giant clockwise arc, over the Indian Ocean, and back toward the coast of Western Australia.

On February 14, 2012, the Fire and Emergency Services Authority (FESA) of Western Australia reported that the bushfires that were burning around Windy Harbour the day before had been contained. Still, FESA warned residents to keep abreast of new developments as conditions could change quickly.

References

FESA. (2012, February 14). Alerts and Warnings. Authority of Western Australia. Accessed February 14, 2012.

NASA image courtesy Jeff Schmaltz, LANCE/EOSDIS MODIS Rapid Response Team at NASA GSFC. Caption by Michon Scott.

Instrument: Aqua - MODIS

http://spaceflight1.nasa.gov/realdata/sightings/cities/view.cgi?country=United_States&region=California&city=Davis

SATELLITE	LOCAL DATE/TIME	DURATION (MIN)	MAX ELEV (DEG)	APPROACH (DEG-DIR)	DEPARTURE (DEG-DIR)
ISS	Wed Feb 15/07:01 PM	3	22	19 above WNW	15 above NNE
ISS	Thu Feb 16/06:06 PM	2	38	38 above N	11 above NE
ISS	Thu Feb 16/07:42 PM	< 1	10	10 above NNW	10 above NNW
ISS	Fri Feb 17/06:44 PM	3	15	11 above NW	10 above NNE
ISS	Sun Feb 19/06:27 PM	1	10	10 above NNW	10 above N
ISS	Thu Feb 23/07:30 PM	< 1	10	10 above N	10 above N
ISS	Sat Feb 25/07:12 PM	2	15	10 above NNW	15 above NNE
ISS	Sun Feb 26/06:17 PM	< 1	11	11 above NNE	10 above NNE
ISS	Sun Feb 26/07:50 PM	1	19	10 above NW	19 above NNW
ISS	Mon Feb 27/06:54 PM	3	23	10 above NNW	21 above NE
ISS	Tue Feb 28/07:33 PM	2	69	13 above NW	69 above WNW
ISS	Wed Feb 29/06:36 PM	5	42	10 above NW	13 above ESE
ISS	Wed Feb 29/08:14 PM	< 1	14	13 above W	14 above WSW

February 16, 2012
Change Detection

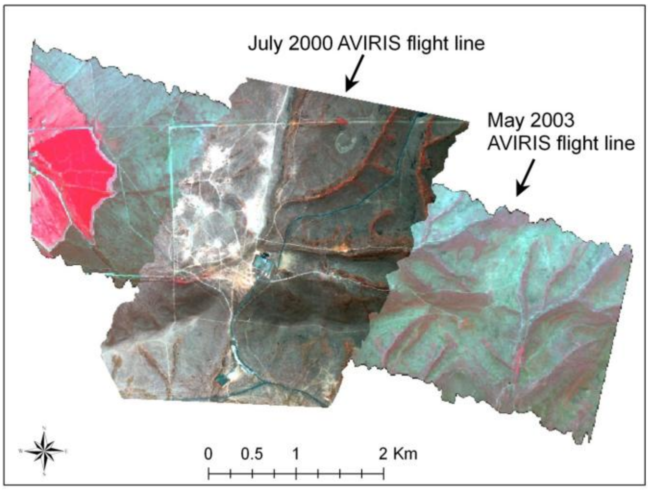

Seasonal, annual, interannual
Phenological patterns; inter-annual to Century-scale patterns
Multitemporal data Change in landscape components,
Phenological patterns; intra-annual to Century-scale patterns
Invasive species mapping Multitemporal data (MODIS, Landsat)
Bidirectional Reflectance Distribution Function (BRDF)

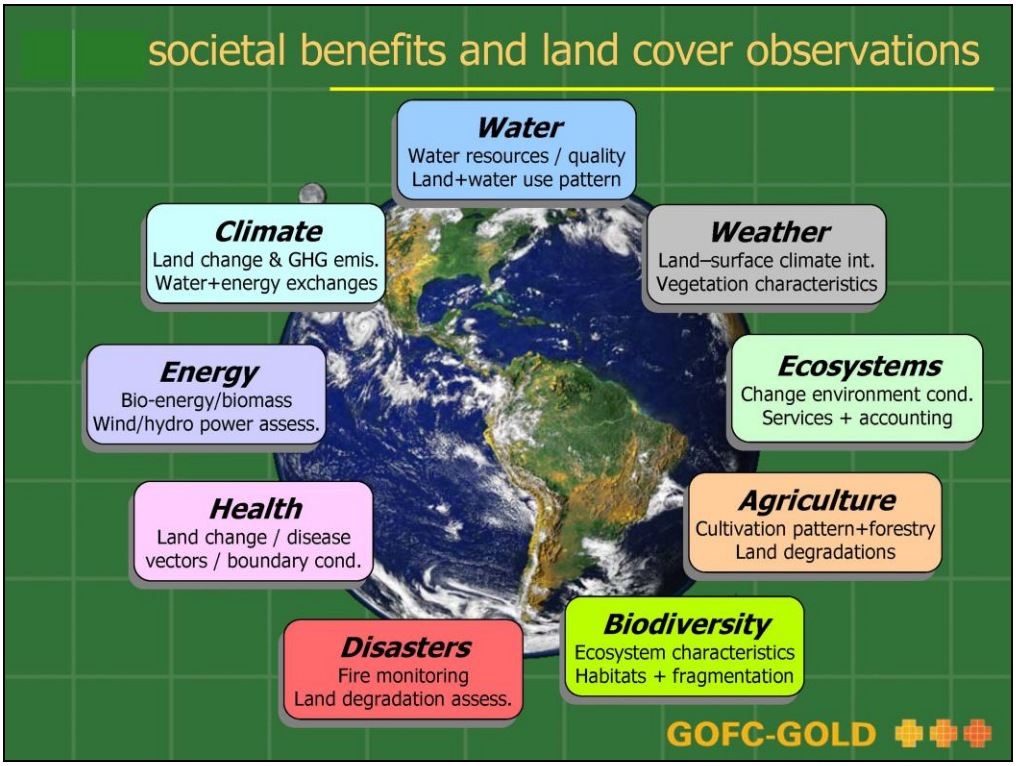
societal benefits and land cover observations
Water
Water resources / quality
Land+water use pattern
Climate
Land change & GHG emis.
Water+energy exchanges
Weather
Land–surface climate int.
Vegetation characteristics
Energy
Bio-energy/biomass
Wind/hydro power assess.
Ecosystems
Change environment cond.
Services + accounting
Health
Land change / disease
vectors / boundary cond.
Agriculture
Cultivation pattern+forestry
Land degradations
Disasters
Fire monitoring
Land degradation assess.
Biodiversity
Ecosystem characteristics
Habitats + fragmentation
GOFC-GOLD

Why is there broad interest in change detection?

Environmental questions Has the habitat deteriorated or become smaller? How close to the urban boundary is high wildfire risk vegetation?

Economic questions Has the area and type of crop production changed in recent years? What is the distance to market?

Societal questions Has the urban area grown? How are parks distributed by population density and income?

Policy questions Should the city annex adjacent farmland for urban expansion?

Police questions Can I locate sites where illegal drugs are being grown?

Political questions What is the social/economic value of land considered for imminent domain? Where should a dam be located?

IPCC 4th assessment report

Table TS.1. *Global carbon budget. By convention, positive values are CO_2 fluxes (GtC yr^{-1}) into the atmosphere and negative values represent uptake from the atmosphere (i.e., 'CO_2 sinks'). Fossil CO_2 emissions for 2004 and 2005 are based on interim estimates. Due to the limited number of available studies, for the net land-to-atmosphere flux and its components, uncertainty ranges are given as 65% confidence intervals and do not include interannual variability (see Section 7.3). NA indicates that data are not available.*

	1980s	1990s	2000–2005
Atmospheric increase	3.3 ± 0.1	3.2 ± 0.1	4.1 ± 0.1
Fossil carbon dioxide emissions	5.4 ± 0.3	6.4 ± 0.4	7.2 ± 0.3
Net ocean-to-atmosphere flux	–1.8 ± 0.8	–2.2 ± 0.4	–2.2 ± 0.5
Net land-to-atmosphere flux	–0.3 ± 0.9	–1.0 ± 0.6	–0.9 ± 0.6
Partitioned as follows			
Land use change flux	1.4 (0.4 to 2.3)	1.6 (0.5 to 2.7)	NA
Residual land sink	–1.7 (–3.4 to 0.2)	–2.6 (–4.3 to –0.9)	NA

[3] Fossil CO_2 emissions include those from the production, distribution and consumption of fossil fuels and from cement production. Emission of 1 GtC corresponds to 3.67 $GtCO_2$.
[4] As explained in Section 7.3, uncertainty ranges for land use change emissions, and hence for the full carbon cycle budget, can only be given as 65% confidence intervals.

Martin Herold, Wageningen University
Co-Chair, GOFC-GOLD Land Cover ECV/ESA-CCI Partner
22March 2011

Crop development in two growing seasons

What differences do you see?

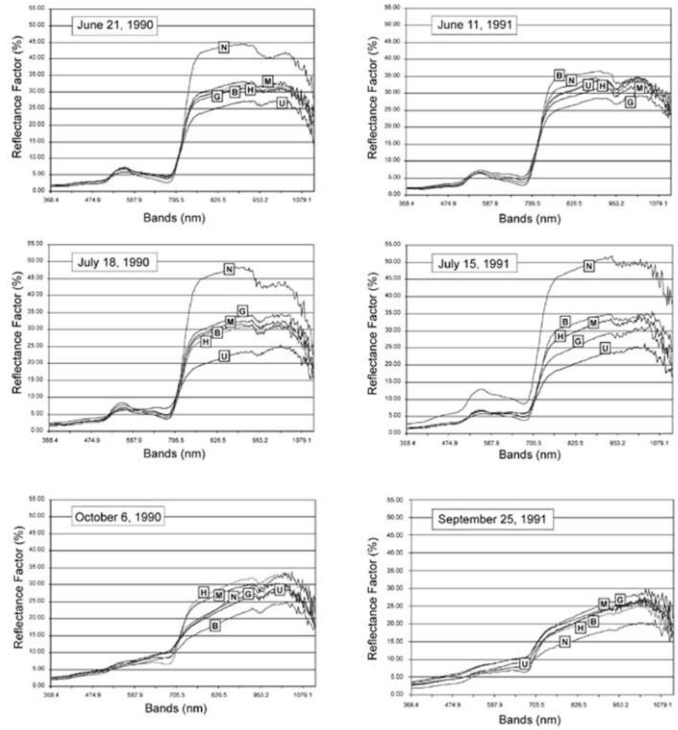

Note changes within growing seasons and between; can you infer differences in weather or management?

Data Distribution in Typical Single-date Image

Data Distribution for a Pixel over Multi-date Images

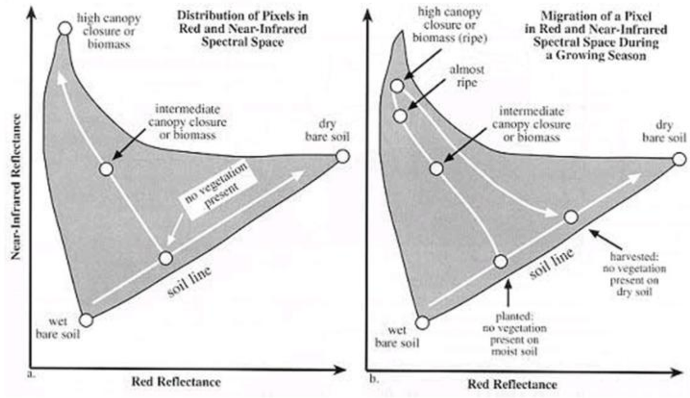

What causes these patterns: characteristics of senescent plants do not follow the same trajectory as the green-up period. Also sun-view angles change with season.

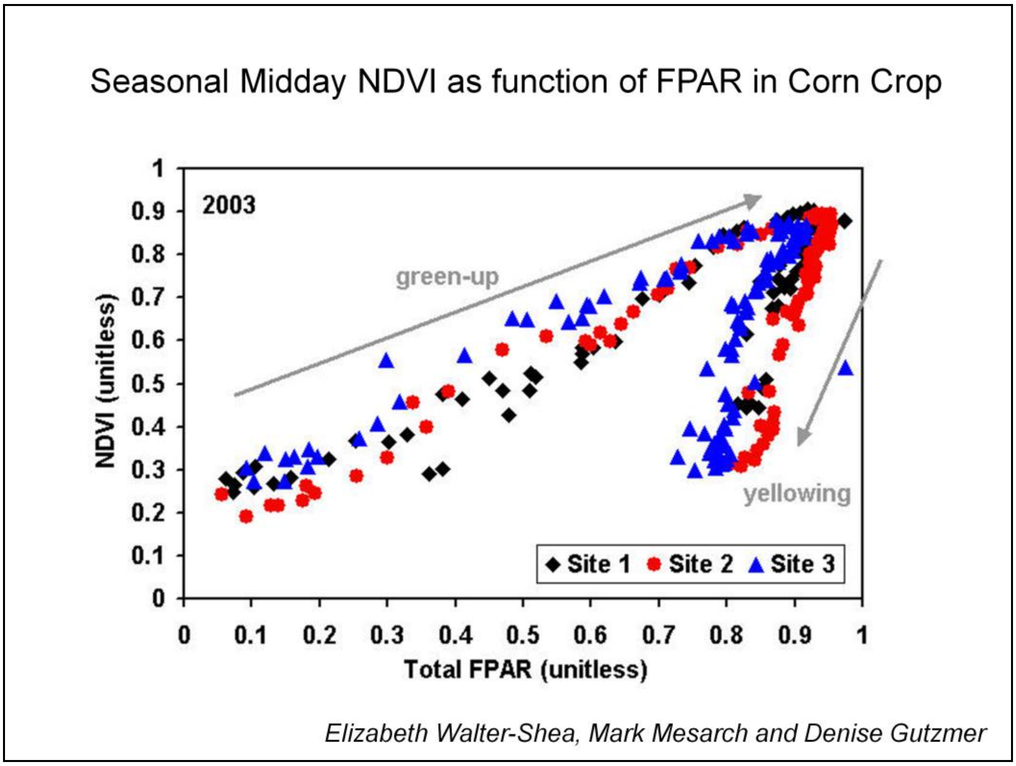

Mid-day values of the remote sensing normalized difference vegetation index [NDVI = [(ρNIR - ρred) / (ρNIR + ρred)] as a function of the total fraction of photosynthetically active radiation absorbed by the corn crop (total FPAR) in 2003. ρNIR is reflectance in the near-infrared spectrum (862-874 nm) and ρred is reflectance in the red portion of the spectrum (665-675 nm). Elizabeth Walter-Shea, Mark Mesarch and Denise Gutzmer

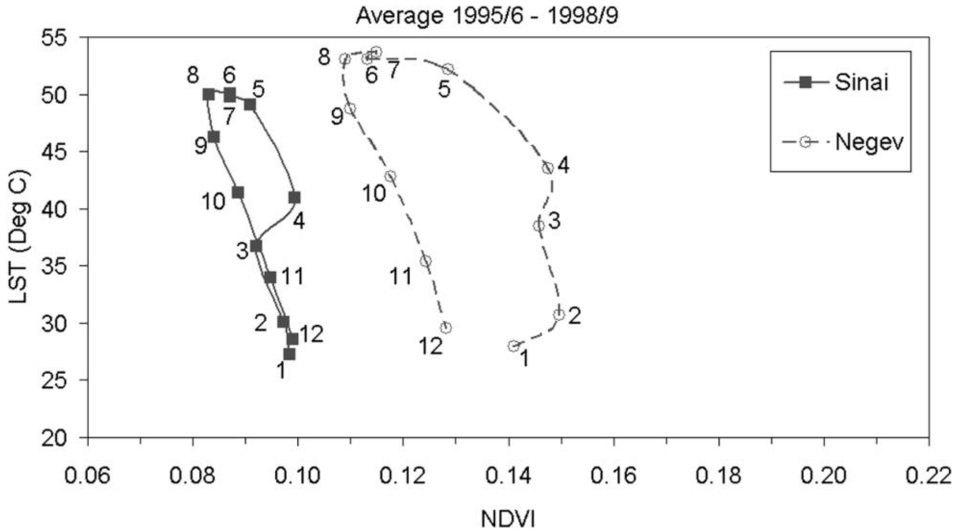

Note: The desertified Sinai ecosystem exhibits the highest variability mostly along the LST axis and is almost unaffected by the NDVI. On the other hand, the recovered Negev side of the border exhibits variability on both LST and NDVI axes

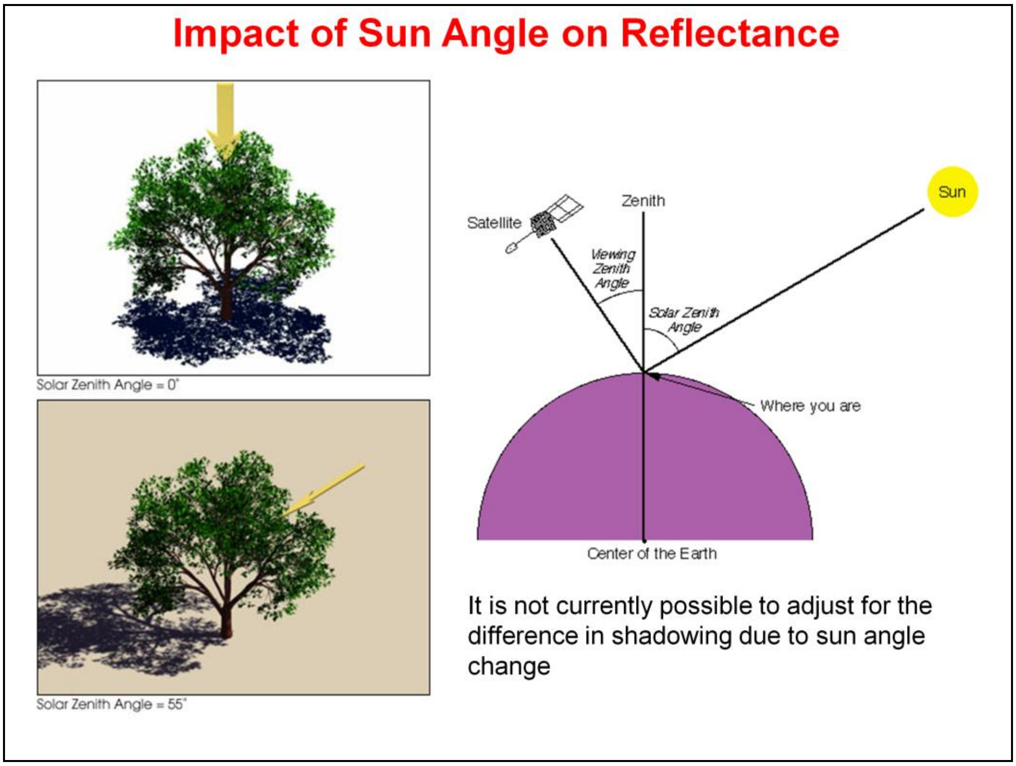

The angle between the sun and the Earth's surface, called solar-zenith angle, changes reflected sunlight in several ways. At low solar zenith angles, such as local noon, top, the sunlight passes through relatively little atmosphere, minimizing **scattering** of **light** by the atmosphere and any effects of pollution, **haze**, or **water vapor**. The sunlight is also perpendicular to the Earth's surface, so it is scattered directly back towards a sensor.

At high solar-zenith angles, like the bottom image (55°), atmospheric scattering is increased, decreasing the amount of shorter **wavelength** light (blue) in incident sunlight. Some surfaces reflect light differently at high angles than low ones. An additional effect is the increase in the apparent depth of forest **canopy** at high angles.

Images by Robert Simmon, NASA GSFC

Canopy shadows change with illumination changes during day and over season

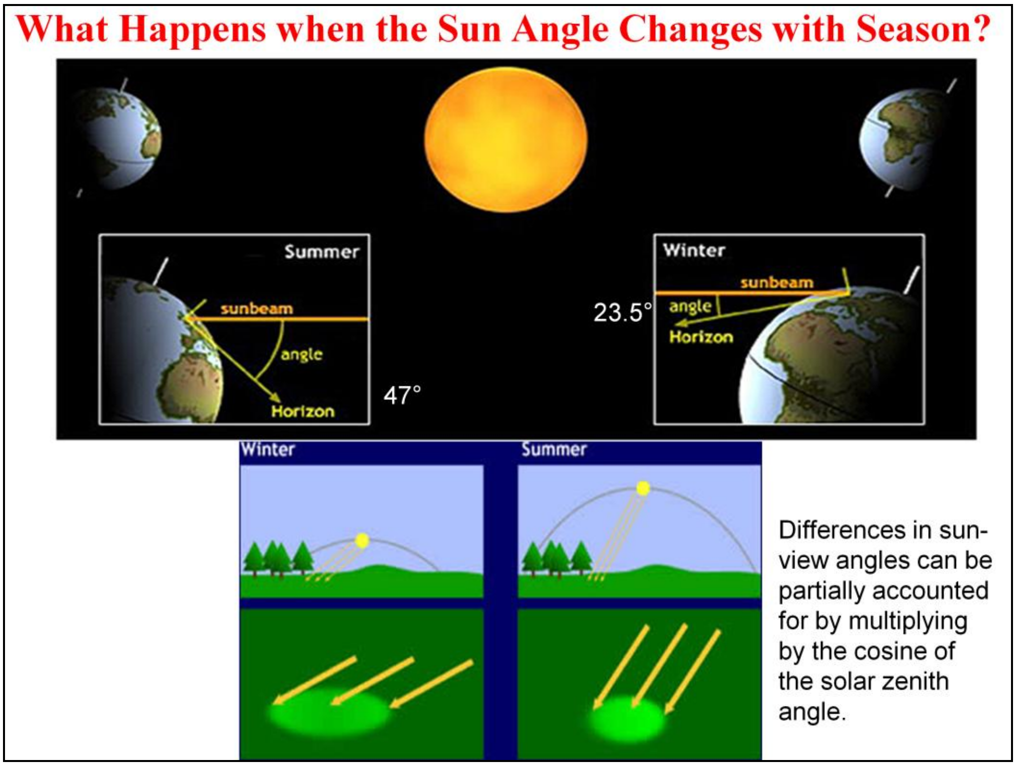

At the Equinoxes, the Earth's equator lies directly beneath the *solar point*. Between Summer and Winter solstices the equator is shifted a total of 2 times 23.5 or 47° over this six month period (the same occurs in the opposite direction between Winter and Summer. This oscillation accounts for the seasons. At intermediate times the heating patterns relative to the Earth's geography tend, on average, to fall between the extremes. In either hemisphere, this next diagram applies.

In the summer case, the angle between a direct line to the Sun and the nearby horizon (Earth's surface meets the atmospheric base in the line of sight) is higher than in the winter case. This simply means that the Sun appears higher in the sky at Noon in Summer than in Winter.

BRDF

Backscatter direction Forward scatter direction

A soybean field. Left: backscattering (sun behind observer). Right: forward scattering (sun opposite observer), note the specular reflection of the leaves. Photograph by Don Deering.

BRDF

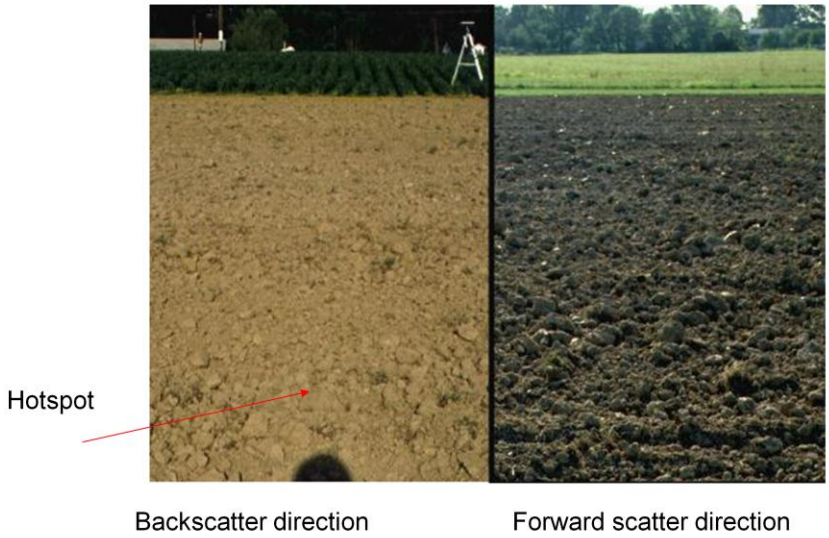

A barren field with rough surface Left: backscattering (sun behind observer), note the bright region (hotspot) where all shadows are hidden. Right: forward scattering (sun opposite observer), note the specular reflection. Photograph by Don Deering.

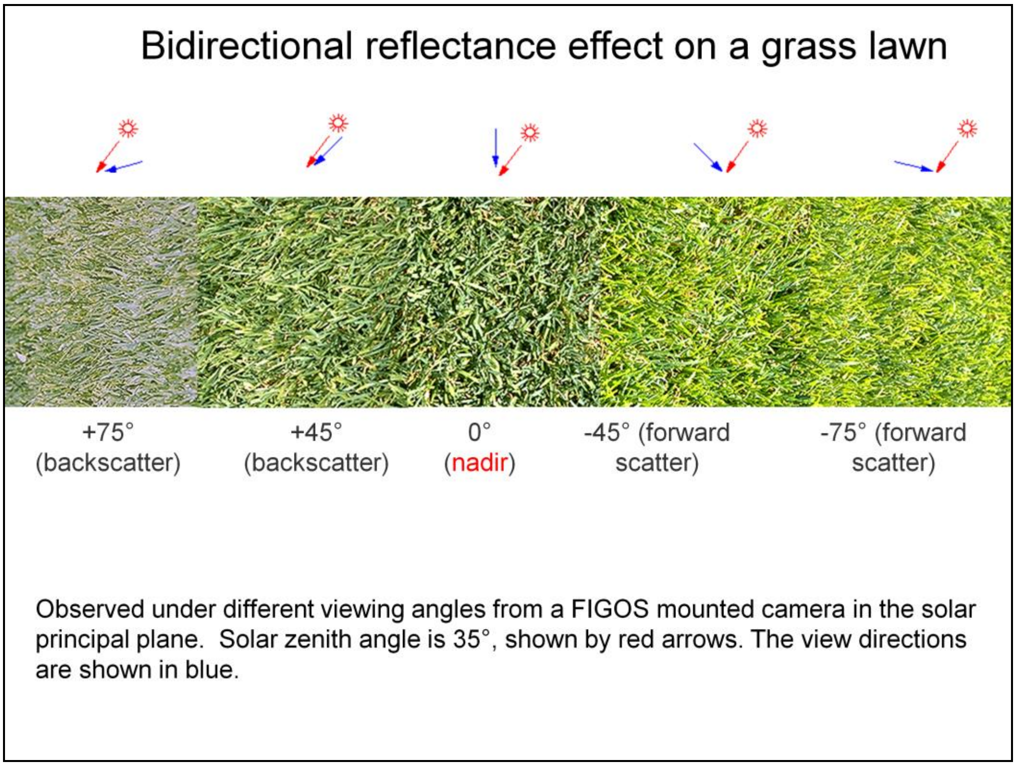

The camera maintained aperture, exposure time and focal length constant (k=16, t=1/15, f=135mm).

Note that nadir = downlooking; normal to horizontal surface

Local Hotspot in Backscatter view

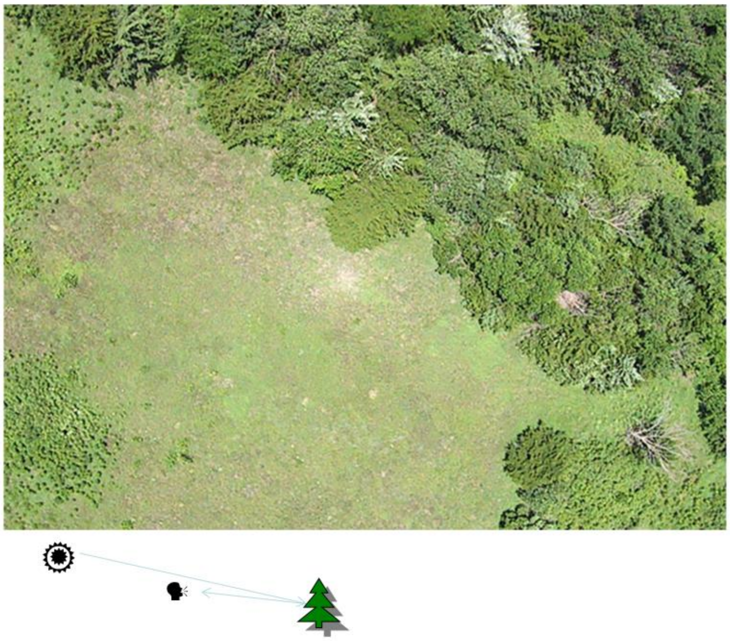

Invariant Targets Used to Assess Differences Between Images due to atmospheric effects, sun angles

Measure transects observed in images to be compared

Use bare pavement, soil, rock outcrop areas to find "invariant targets"

Most Common Change Detection Methods

1. Visual Comparison
2. Superimpose images to visualize
3. Subtract one image by another (identical if 0; range +1 to -1)
4. Ratio images (identical if 1; range from + to -)
5. Pre- classification change detection
6. Post-classification change detection

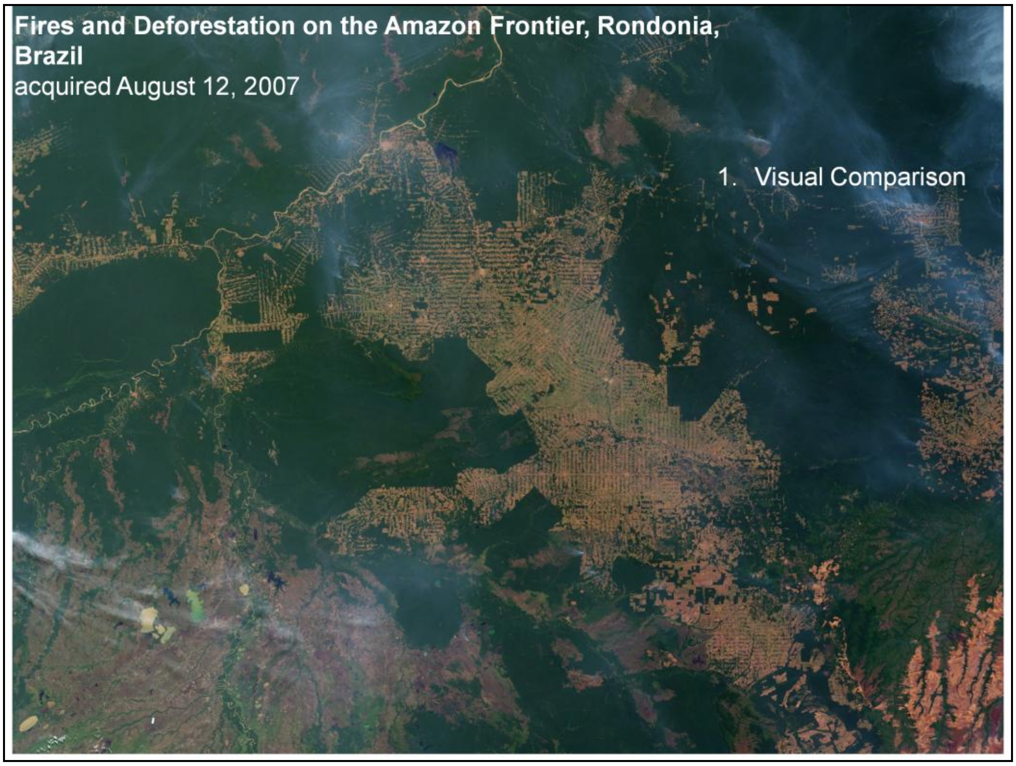

In the image from August 12, 2007, intact forest is deep green, while cleared areas are tan (bare ground) or light green (crops, pasture, or occasionally, second-growth forest). This image is one of ten images in the Earth Observatory's World of Change: Amazon Deforestation article.

The fishbone pattern of small clearings along new roads is the beginning of one of the common deforestation trajectories in the Amazon. New roads (legal and illegal) attract small farmers, who clear some land for crops. When the soil gives out, they convert the old croplands to pasture and clear new forest. When yields fall again and not enough forest remains to clear, they sell or abandon their small holdings to larger-scale ranchers, who consolidate the small farms into large pastures.

References

Pedlowski, M., Dale, V., Matricardi, E., and da Silva Filho, E. (1997). Patterns and impacts of deforestation in Rondônia, Brazil. *Landscape and Urban Planning,* 38, 149–157.

NASA images by Jesse Allen and Robert Simmon, based on data from the MODIS science team. Caption by Rebecca Lindsey.

Instrument: Terra - MODIS

The state of Rondônia in western Brazil is one of the most deforested parts of the Amazon. By the beginning of this decade, the frontier had reached the remote northwest corner of Rondônia, pictured in this pair of images from the Moderate Resolution Imaging Spectroradiometer (MODIS) on NASA's Terra satellite from 2007.

The image from September 30, 2007, shows one consequence of forest clearing in the Amazon: thick smoke that hangs over the forest at different times throughout the dry season. Fire is the primary tool for clearing land in the Amazon, and it doesn't always stay where land owners intend it to. It frequently escapes control and invades adjacent forest and pasture. In 2007, the biomass burning season in the Amazon was the most intense of this decade. This smoky sight was common throughout August and September.

References

Pedlowski, M., Dale, V., Matricardi, E., and da Silva Filho, E. (1997). Patterns and impacts of deforestation in Rondônia, Brazil. *Landscape and Urban Planning,* 38, 149–157.

NASA images by Jesse Allen and Robert Simmon, based on data from the MODIS science team. Caption by Rebecca Lindsey.

Instrument: Terra - MODIS

GV and NPV over 3 Years in Santa Monica Mountains

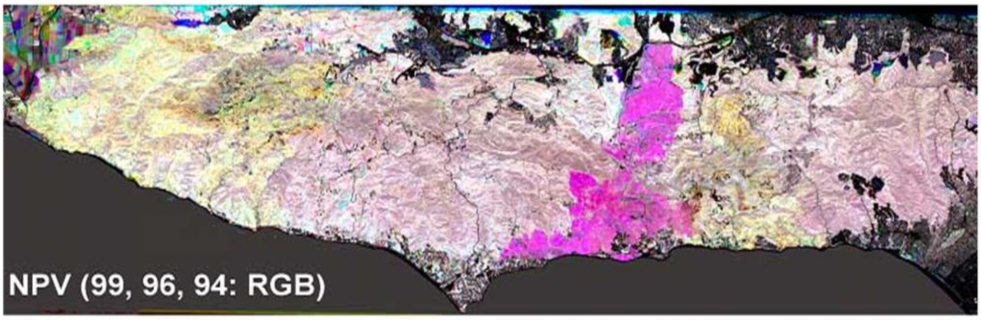

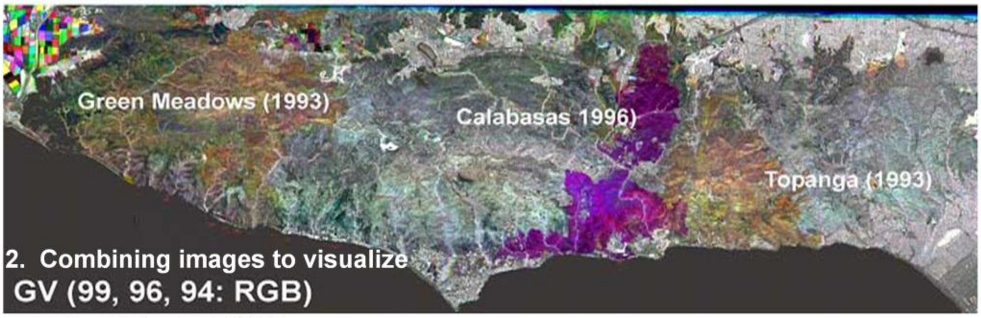

Dar Roberts, UCSB

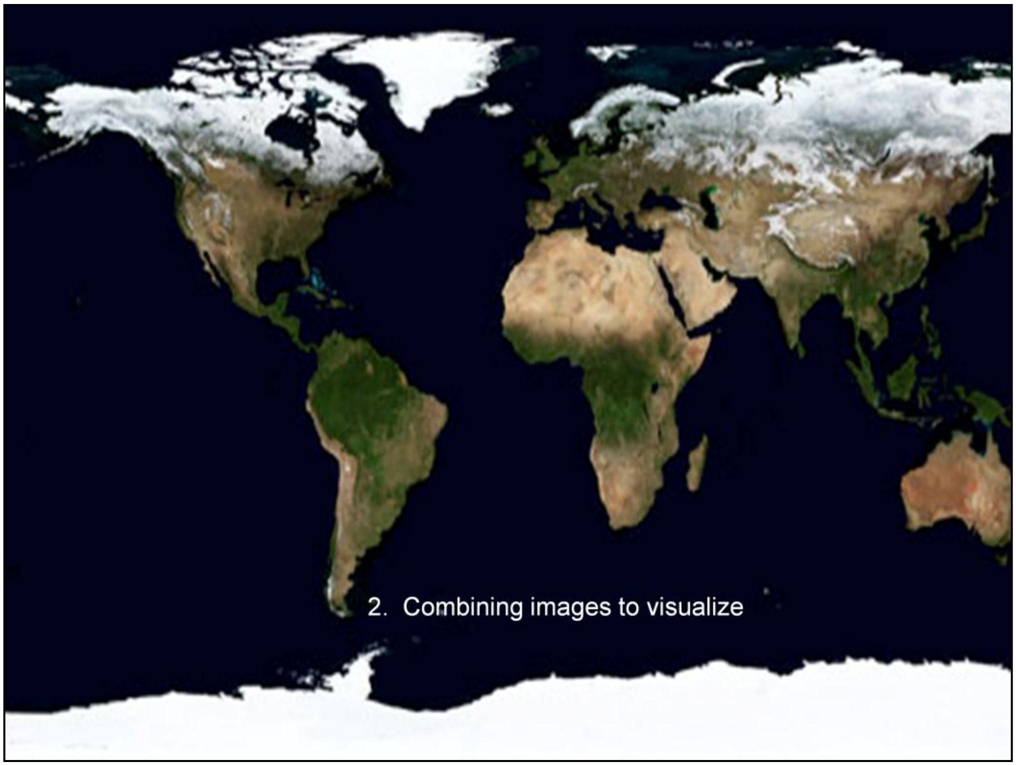

NASA MODIS website;

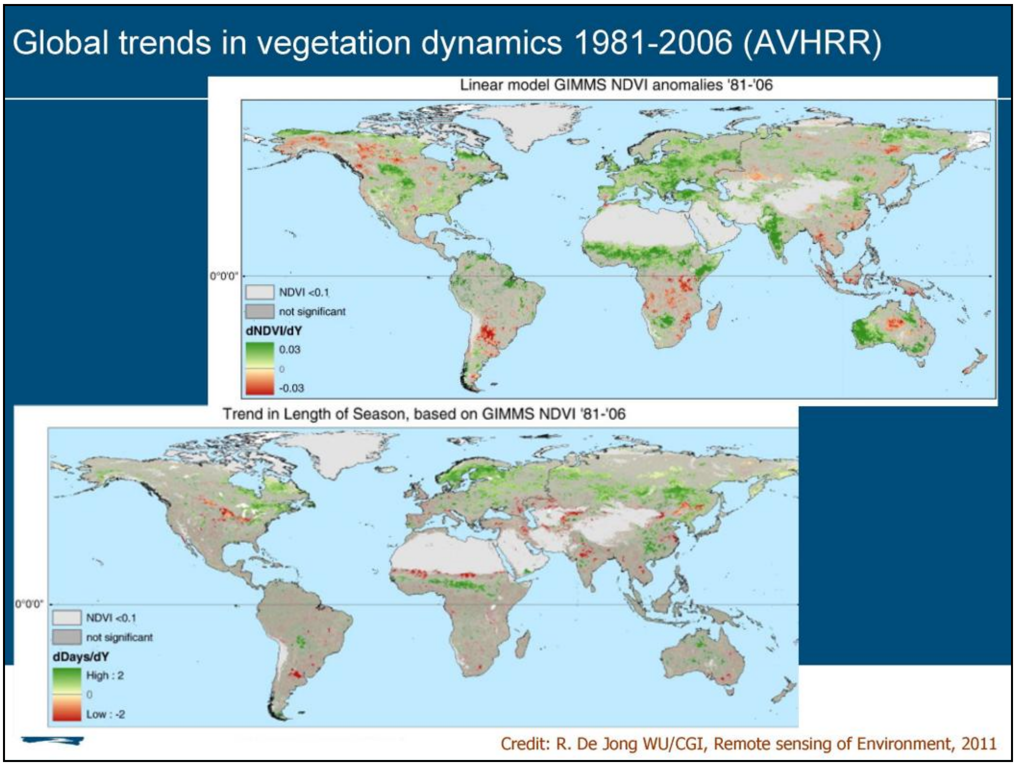

GIMMS (Global Inventory Modeling and Mapping Studies) data set is a normalizeed difference vegetation index (NDVI) product available for a 25 year period spanning from 1981 to 2006. The data set is derived from imagery obtained from the Advanced Very High Resolution Radiometer (AVHRR) instrument onboard the NOAA satellite series 7, 9, 11, 14, 16, and 17. This is an NDVI dataset that has been corrected for calibration, view geometry, volcanic aerosols, and other effects not related to vegetation change.

Figures are from R. DeJong et al. 2011. Remote Sensing of Environment 115: 692-702.

1. Calculate long term trend and identify yearly anomalies.

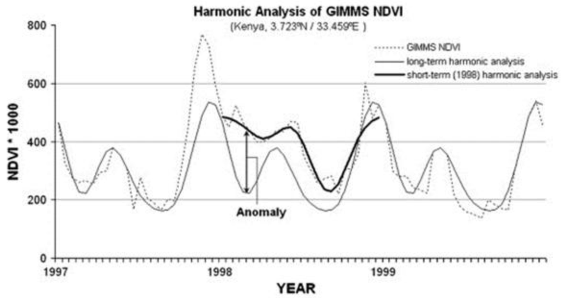

2. Calculate within year variability.

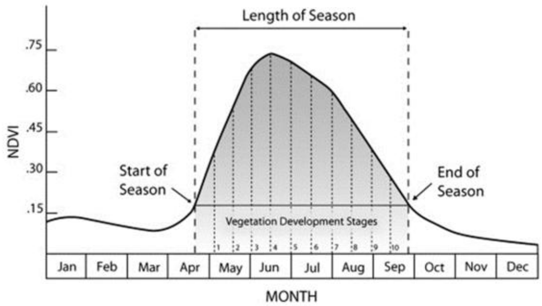

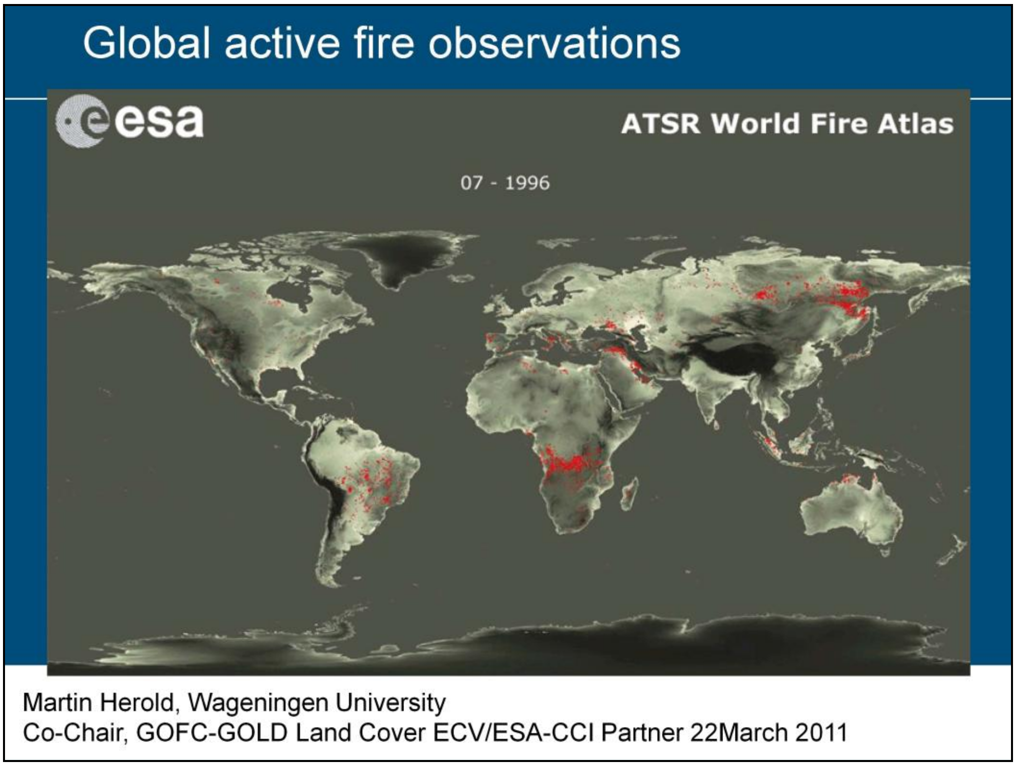

The Along Track Scanning Radiometers (ATSR) are multi-channel imaging radiometers operated by the European Space Agency with the principal objective of providing data concerning global Sea Surface Temperature (SST) to the high levels of accuracy and stability required for monitoring and carrying out research into the behavior of the Earth's climate. The ATSRs are a series of 'Announcement of Opportunity' (AO) instruments, jointly funded by the UK and Australia and flying on board the European Space Agency's ERS-1, ERS-2 and Envisat satellites. The first in the series was designated ATSR-1, the second ATSR-2 and the currently operational instrument is the third in the series, the Advanced ATSR (AATSR). The fourth ATSR, called the Sea and Land Surface Temperature Radiometer (SLSTR), is funded and developed directly by ESA and will be flown on ESA's Sentinel-3 satellite (to be launched in 2013).

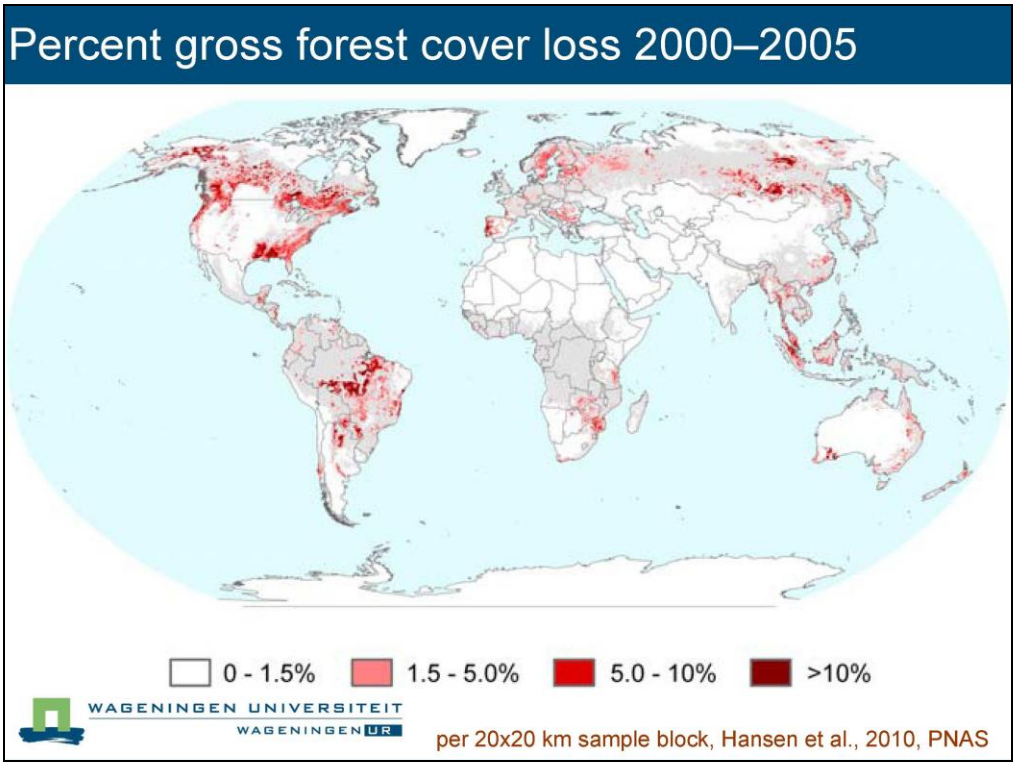

MC Hansen et al. 2010. PNAS May 11, 2010 vol. 107no. 19: 8650-8655. The methodology is based on a stratified random sample of 541 18.5-km × 18.5-km blocks (a sampling density of 0.22%) and employs data from two satellite-based sensors. Coarse spatial resolution data from the MODIS (Moderate Resolution Imaging Spectroradiometer) sensor enable the stratification of the earth's forested biomes into regions of homogeneous

forest cover loss. Landsat Enhanced Thematic Mapper Plus (ETM+) data obtained for the sampled blocks were then used to quantify area of year 2000 forest and area of GFCL.

3. Subtract one image by another (identical if 0; range +1 to -1)

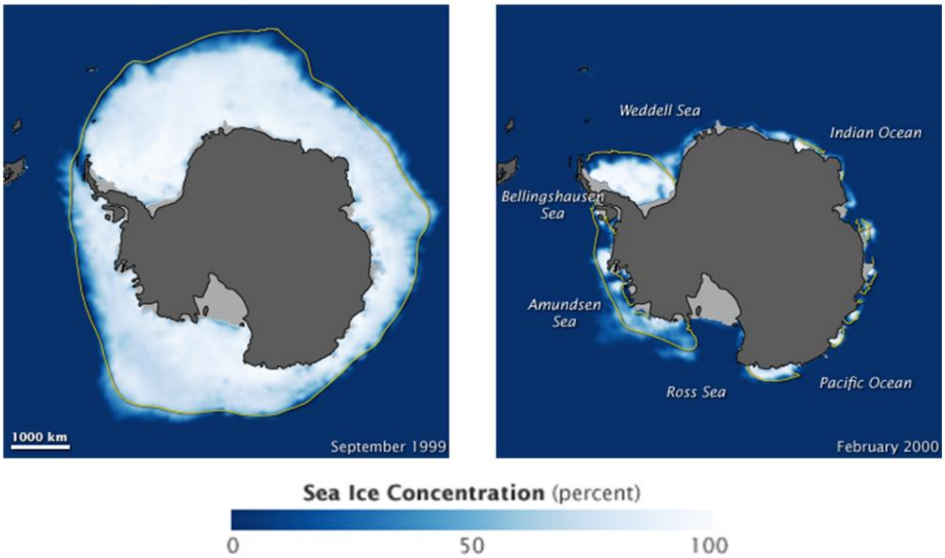

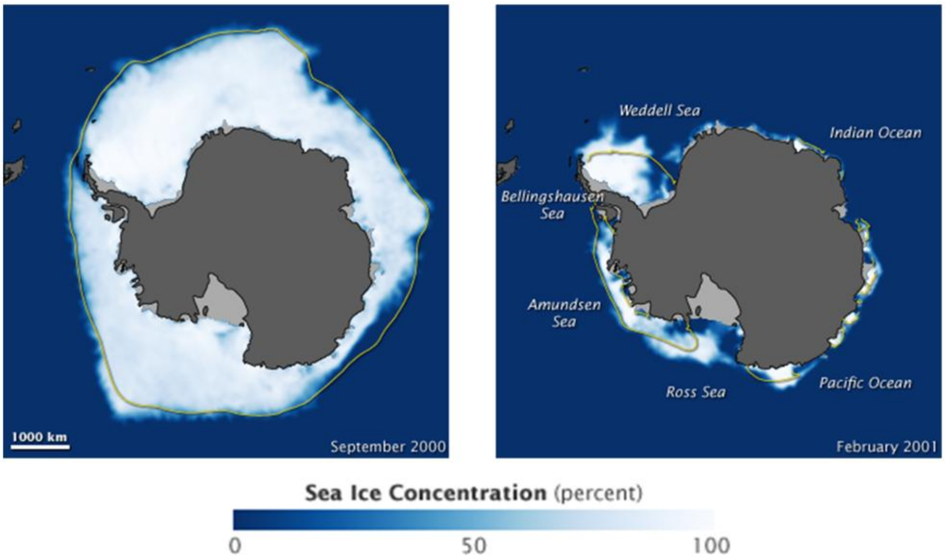
1000 km
September 2000
Weddell Sea
Indian Ocean
Bellingshausen Sea
Amundsen Sea
Ross Sea
Pacific Ocean
February 2001
Sea Ice Concentration (percent)
0
50
100

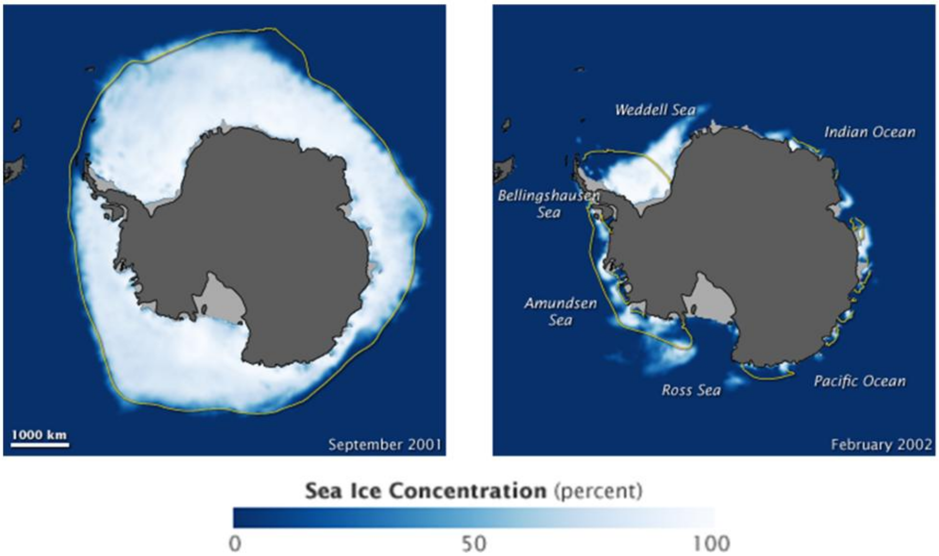
Weddell Sea
Indian Ocean
Bellingshausen Sea
Amundsen Sea
Ross Sea
Pacific Ocean
1000 km
September 2001
February 2002
Sea Ice Concentration (percent)
0
50
100

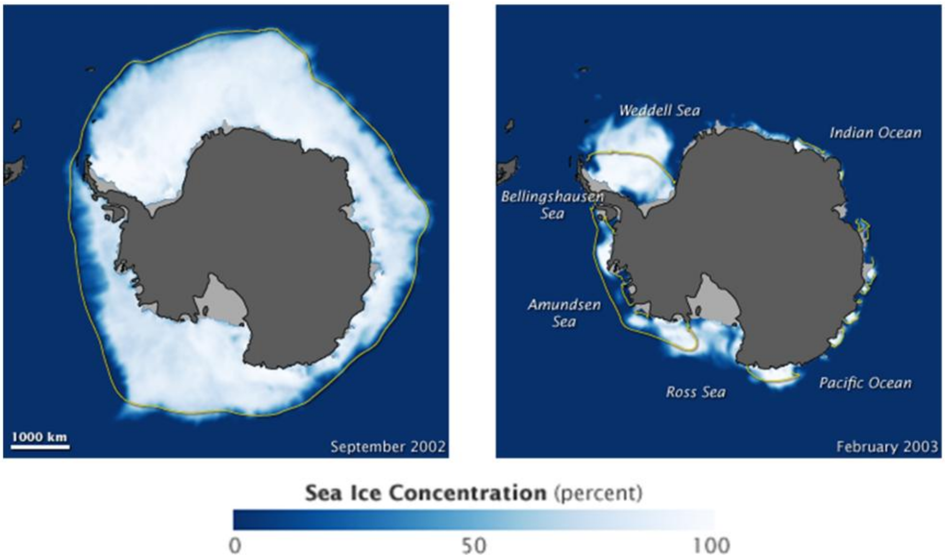

1000 km
September 2002
Weddell Sea
Indian Ocean
Bellingshausen Sea
Amundsen Sea
Ross Sea
Pacific Ocean
February 2003
Sea Ice Concentration (percent)
0
50
100

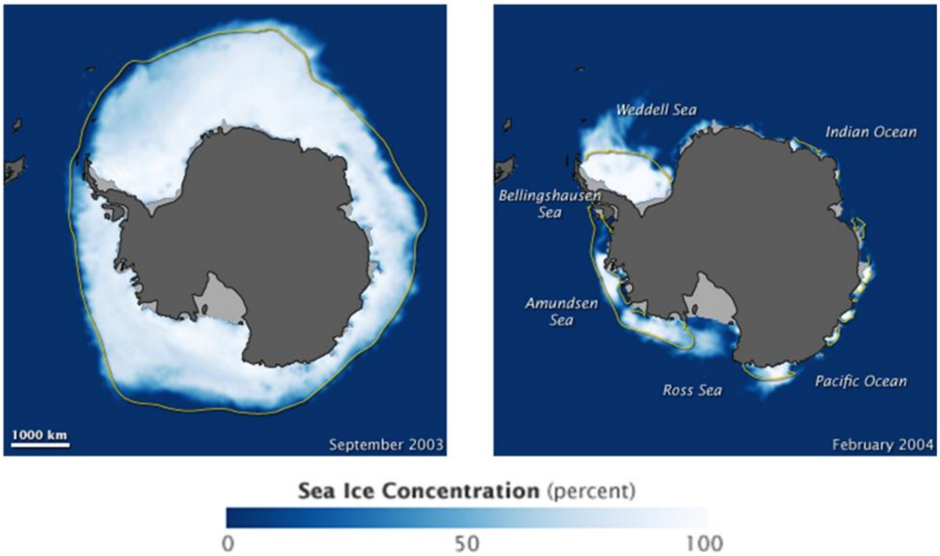

1000 km
September 2003
Weddell Sea
Indian Ocean
Bellingshausen Sea
Amundsen Sea
Ross Sea
Pacific Ocean
February 2004
Sea Ice Concentration (percent)
0
50
100

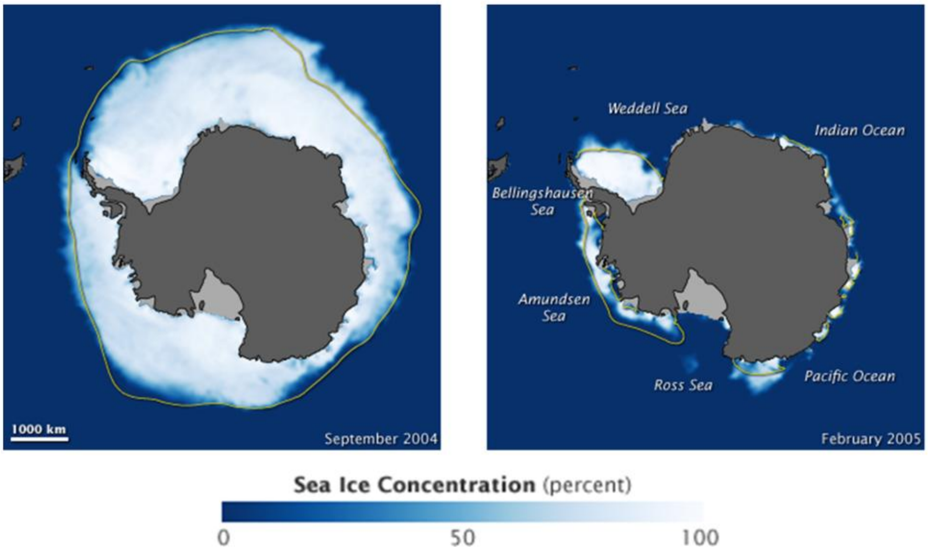
Weddell Sea
Indian Ocean
Bellingshausen Sea
Amundsen Sea
Ross Sea
Pacific Ocean
1000 km
September 2004
February 2005
Sea Ice Concentration (percent)
0
50
100

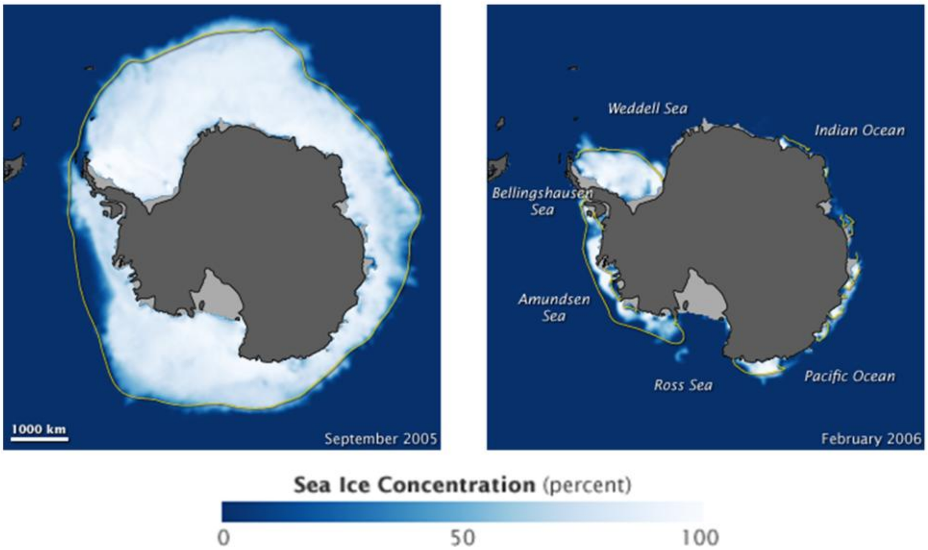
Weddell Sea
Indian Ocean
Bellingshausen Sea
Amundsen Sea
Ross Sea
Pacific Ocean
1000 km
September 2005
February 2006
Sea Ice Concentration (percent)
0
50
100

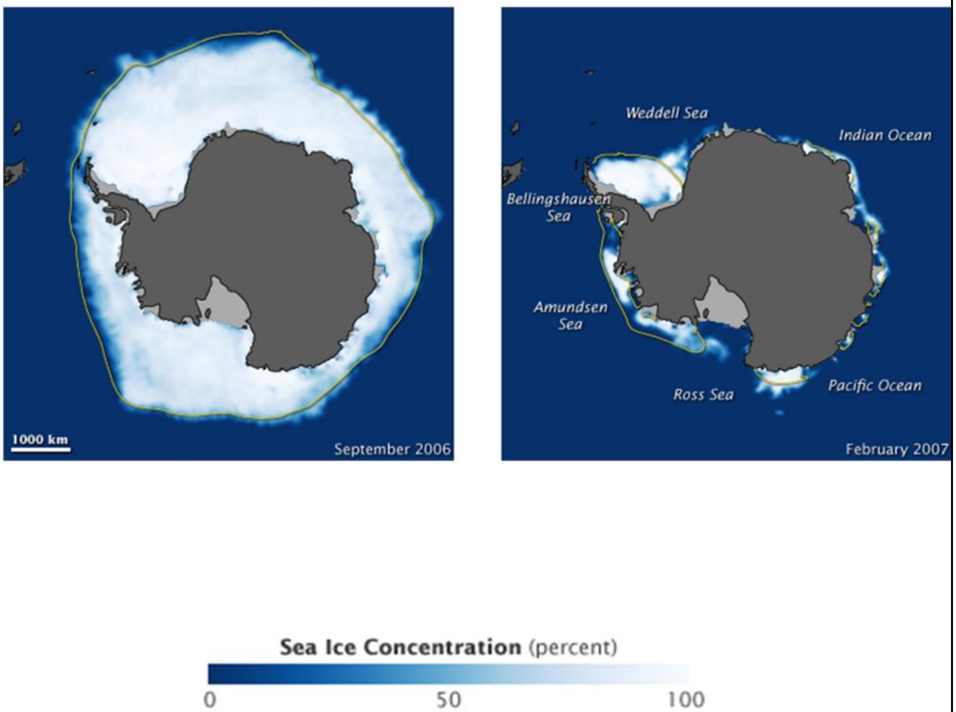

1000 km
September 2006
Weddell Sea
Indian Ocean
Bellingshausen Sea
Amundsen Sea
Ross Sea
Pacific Ocean
February 2007
Sea Ice Concentration (percent)
0
50
100

South Pole Sea Ice at 2008 Maximum and 2009 Minimum

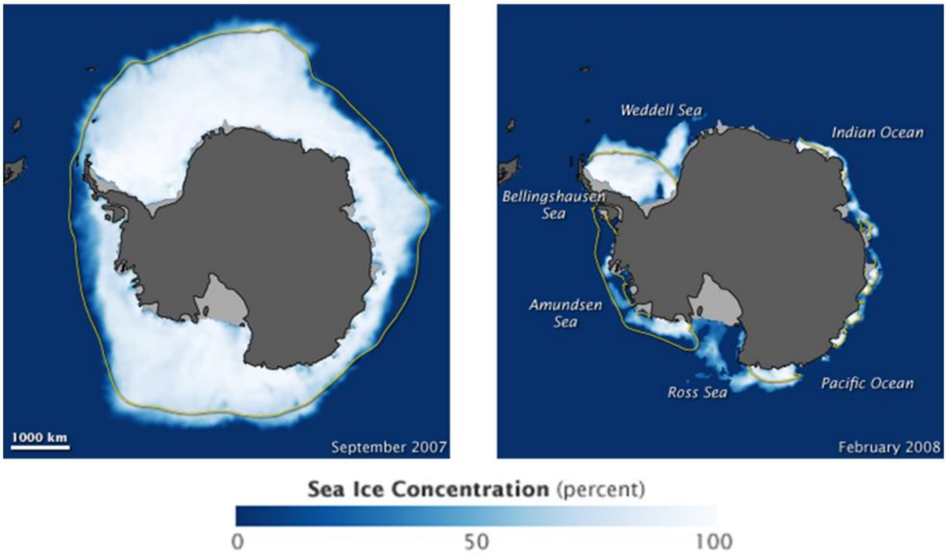

Posted May 23, 2009

4. Ratio images (identical if 1; range from + to -)

Ratio Methods

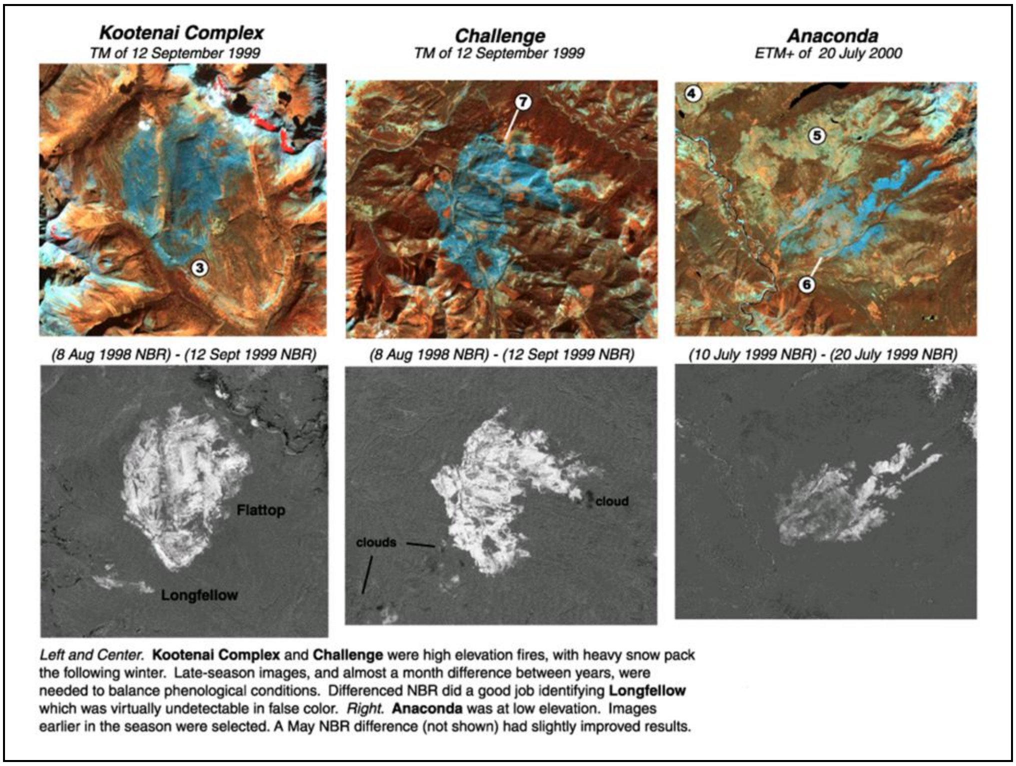

Fire scars before and after fire.

Used NBR (Normalized Burn Ratio)

Note different calendar dates? Why?

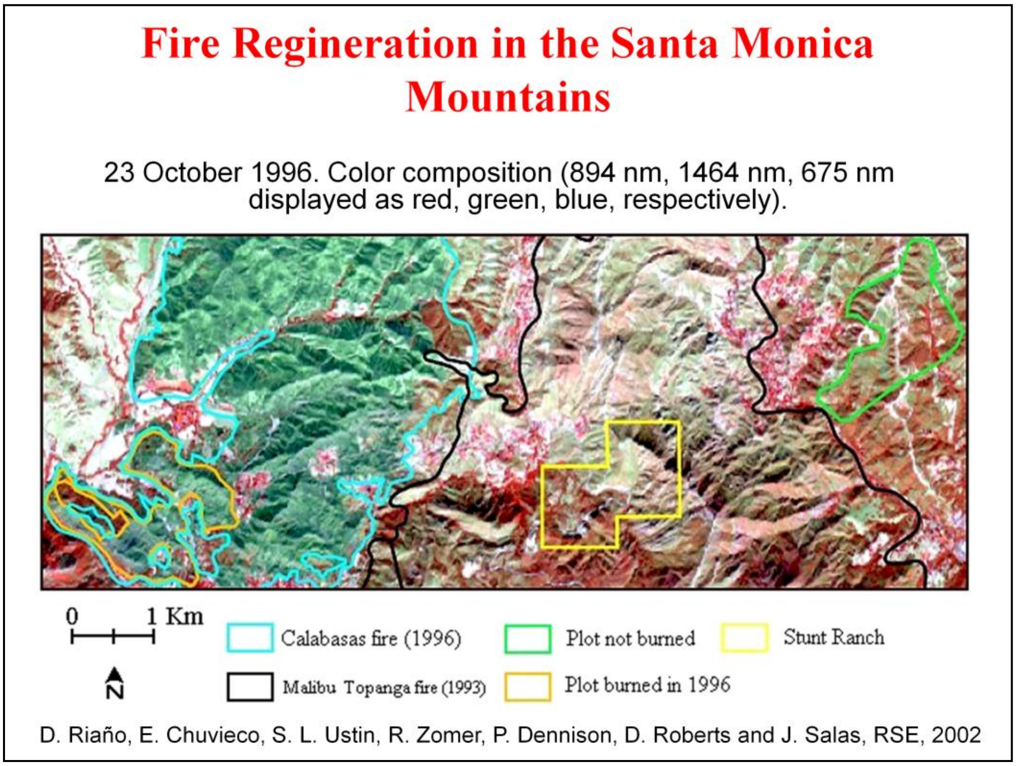

Regeneration patterns after fire in two semi-arid shrub communities: Northern mixed chaparral and Coastal sage scrub.

Revegetation after fire

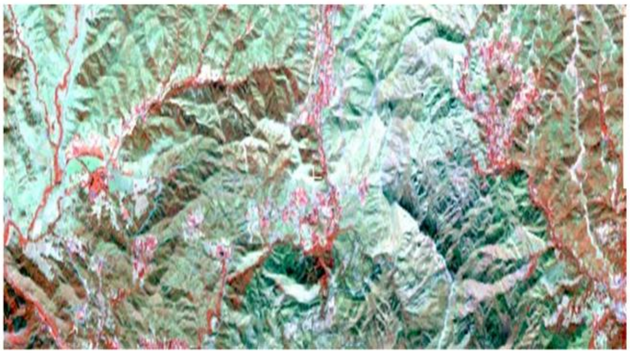

18 May 1998

$$NRI_{VI} = 1 + \frac{VI_{fire} - VI_{control}}{VI_{fire} + VI_{control}} = \frac{2VI_{fire}}{VI_{fire} + VI_{control}}$$

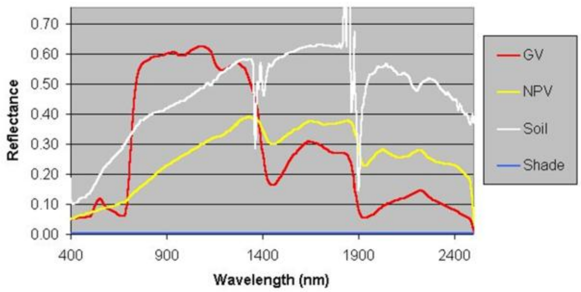

D. Riaño et al., RSE, 2002

An unburned control plot having similar environmental features was employed to generate relative fire regeneration indices

Indices were calculated using the SMA Green Vegetation (GV) endmember and the NDVI.

Estimated Revegetation Time

		Equations	$RI_{VI}=\alpha+\beta \log t$		$NRI_{VI}=\alpha+\beta \log t$	
		Slope	Intercept	R-Pearson	Initial state	Regeneration Time(years)
Northern	RI_{GV}	0.097	0.091	0.89	0.98	26.1
Mixed	NRI_{GV}	0.089	0.240	0.93	0.99	11.9
Chaparral	RI_{NDVI}	0.067	0.359	0.90	0.97	28.0
	NRI_{NDVI}	0.050	0.552	0.94	0.99	16.0
Coastal	RI_{GV}	0.102	0.194	0.97	0.98	6.0
Sage	NRI_{GV}	0.093	0.311	0.96	0.99	3.9
Scrub	RI_{NDVI}	0.034	0.486	0.61	0.84	88.1
	NRI_{NDVI}	0.026	0.651	0.64	0.91	52.2

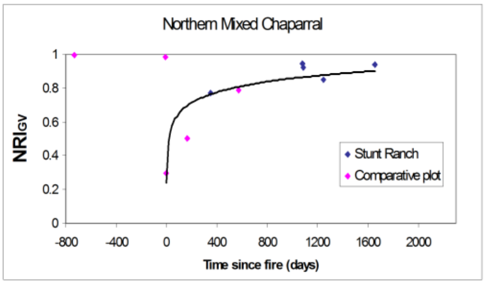

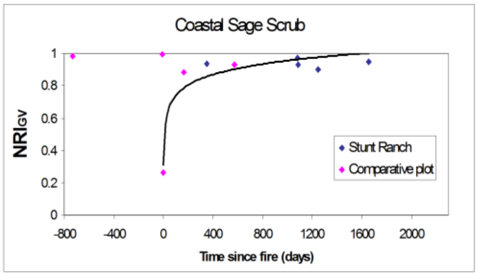

D. Riaño et al., RSE, 2002

Normalized Regeneration Index using SMA Green Vegetation endmember (NRIGV) produced the best estimate for the time to recovery in both communities, based on recovery times in the literature.

The use of NDVI worked well for recovery in the Northern mixed chaparral, but was less successful in the coastal sage scrub, mainly because of extensive herbaceous cover in early years of the regeneration process.

Matching burns in different years to plots having similar environmental features improved estimates of recovery

Simple Relationships: Band Ratios

$$NDVI = \frac{\rho_{NIR} - \rho_R}{\rho_{NIR} + \rho_R}$$

$$NDII_5 = \frac{\rho_{NIR} - \rho_{SWIR,5}}{\rho_{NIR} + \rho_{SWIR,5}}$$

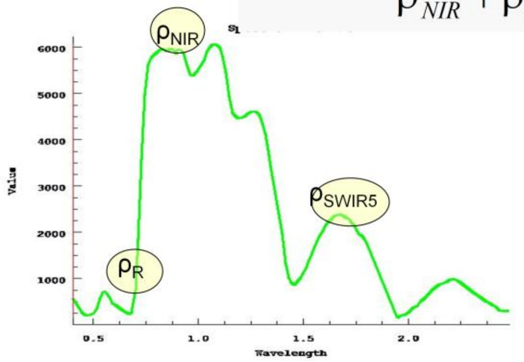

Comparison to sites with different cover

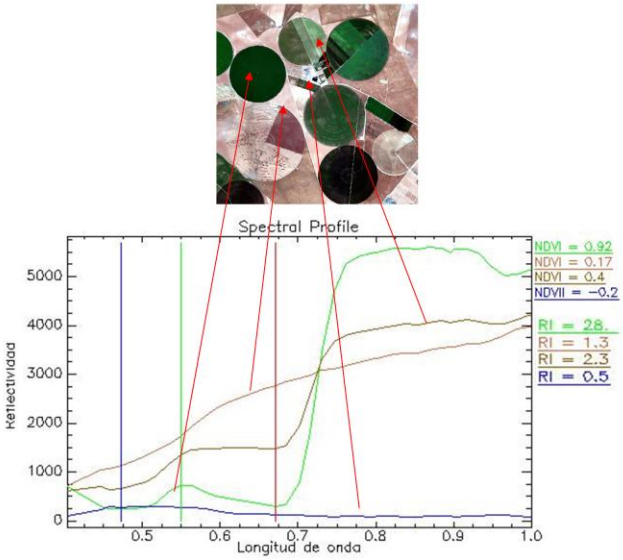

NDVI

SR

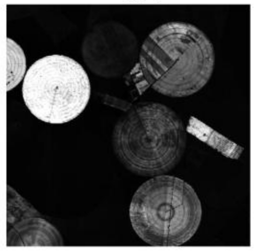

Time series analysis and trends in vegetation

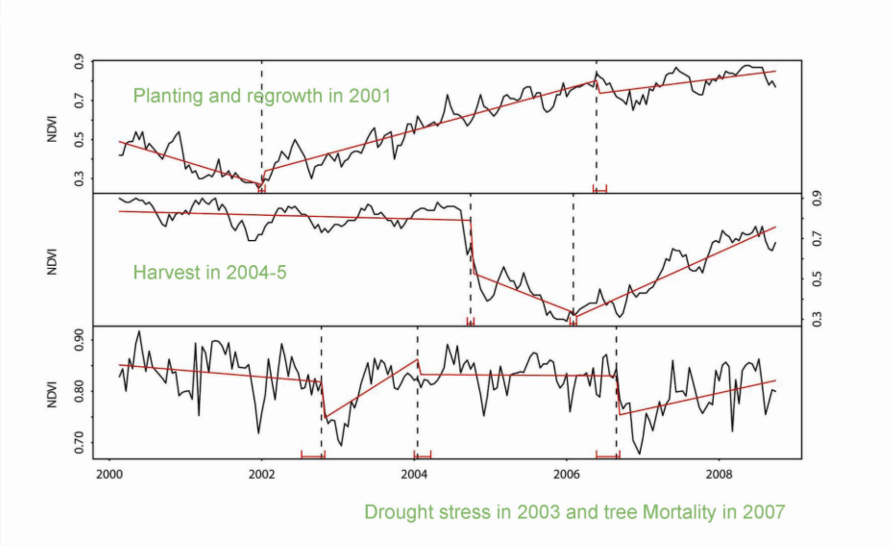

Martin Herold, Wageningen University, Co-Chair, GOFC-GOLD
Land Cover ECV/ESA-CCI Partner 22March 2011

Credit: J. Verbesselt WU/CGI

Modeling Time Series Data to Characterize Phenological Changes

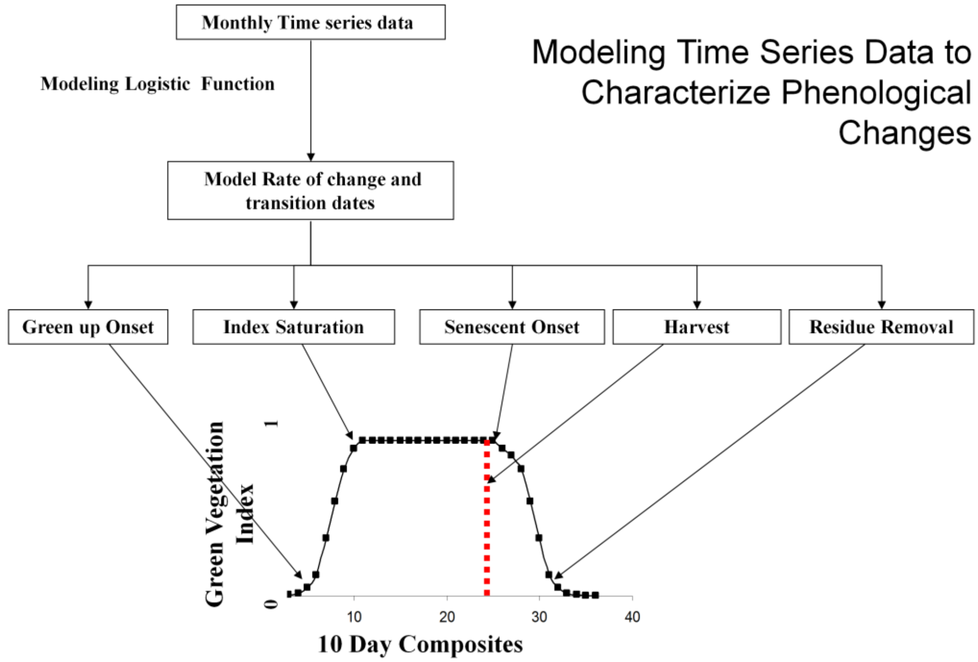

Regional Based Approach: Multiyear time series to model spectral curves for pixel aggregations

Multi-Temporal Profiles of Crop Growth with Same Crop and Different Crops in Two Years

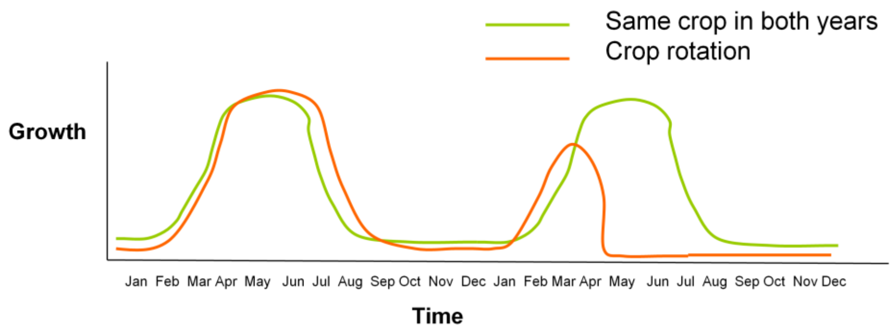

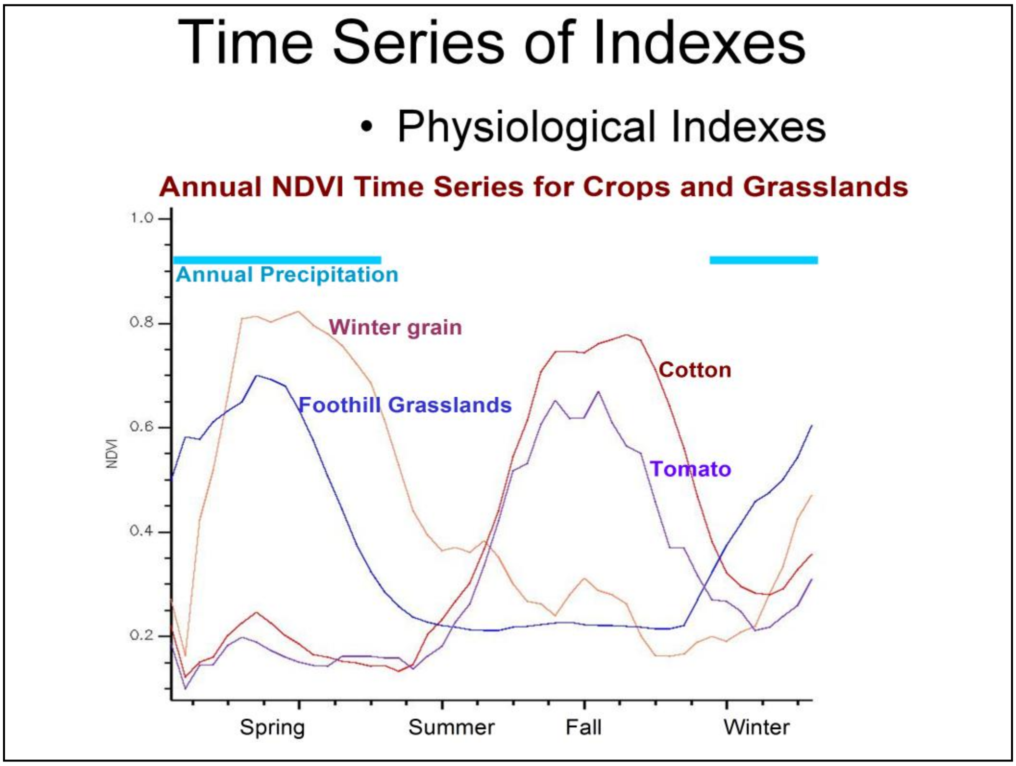

Annual NDVI time series for precipitation dependent winter growth (grains and grasslands) and irrigated summer crops.

Annual Changes in NDVI

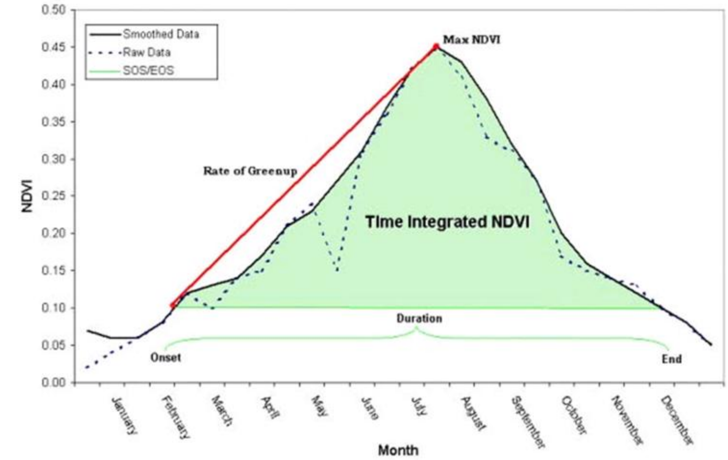

Plant Spectra at Different Resolutions

- Position of Spectral Bands

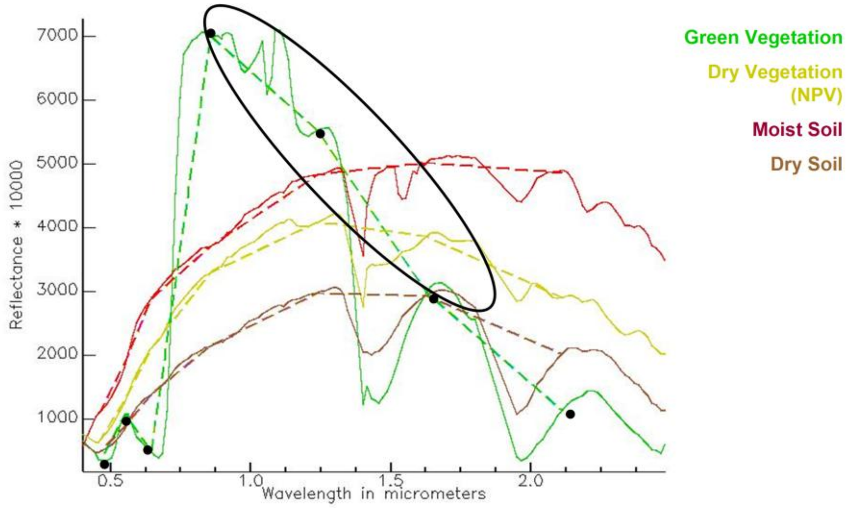

RGLDD-Palacios-Orueta et al. 2005

Spectral Signature for Moist and Dry Soil

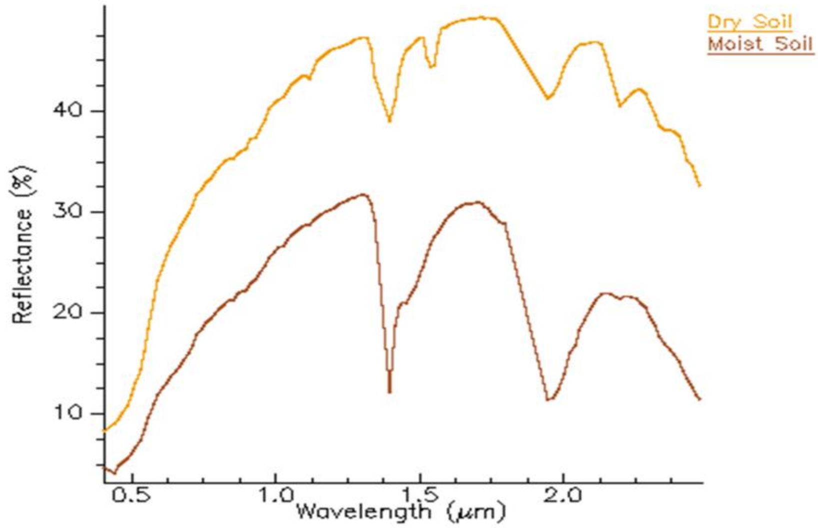

Evolution from Soil to Full Green Cover

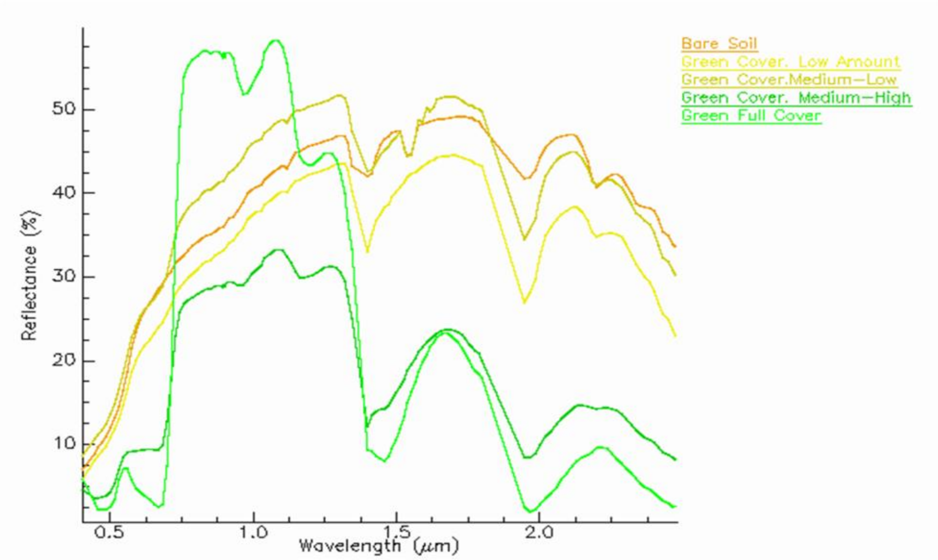

Extracting Spectral Information

- Methods of Spectral Analysis

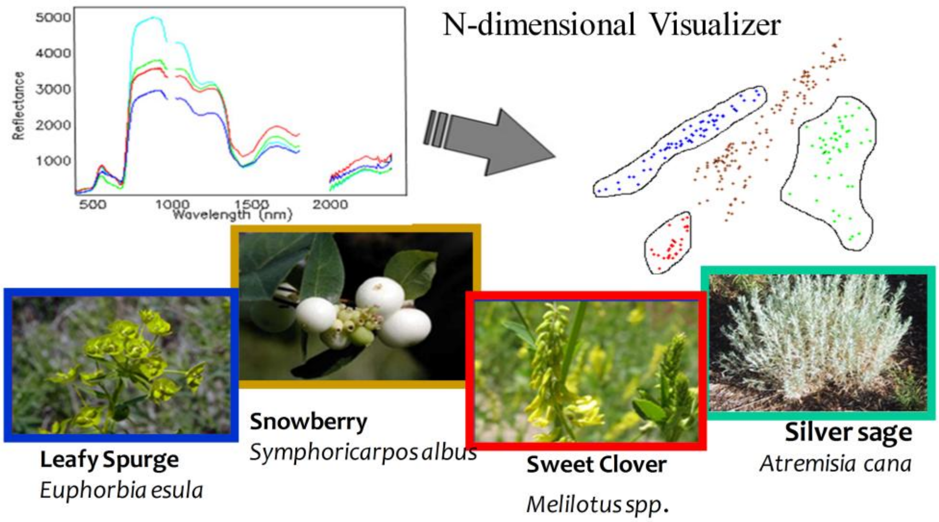

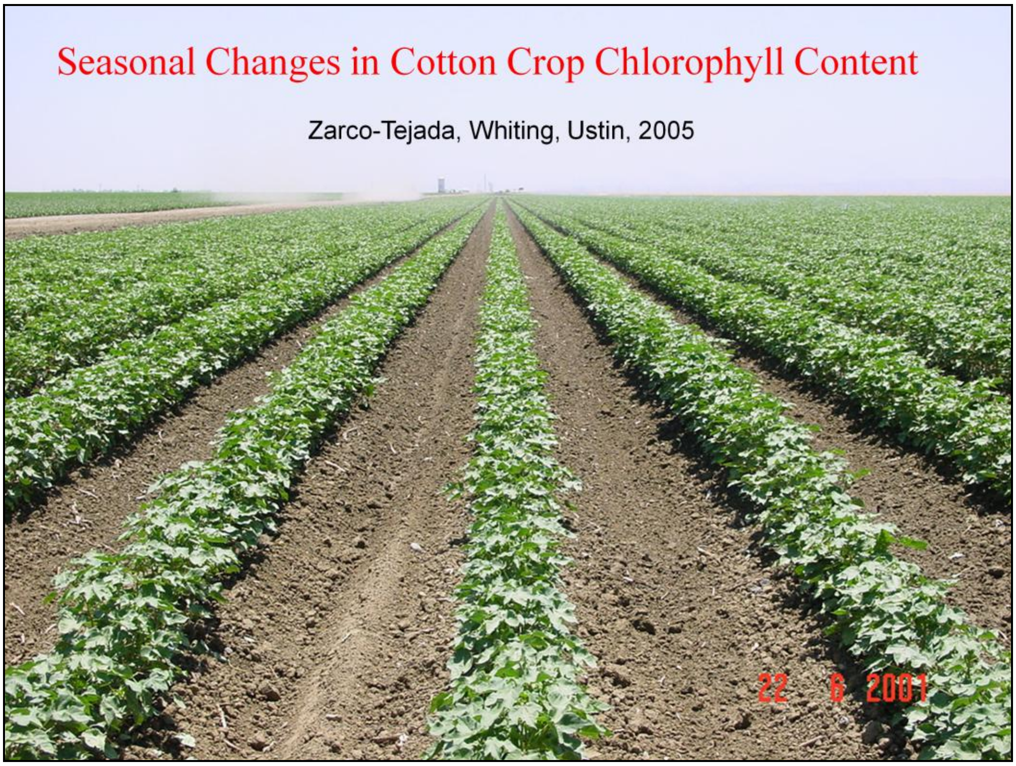
Seasonal Changes in Cotton Crop Chlorophyll Content
Zarco-Tejada, Whiting, Ustin, 2005
22 6 2001

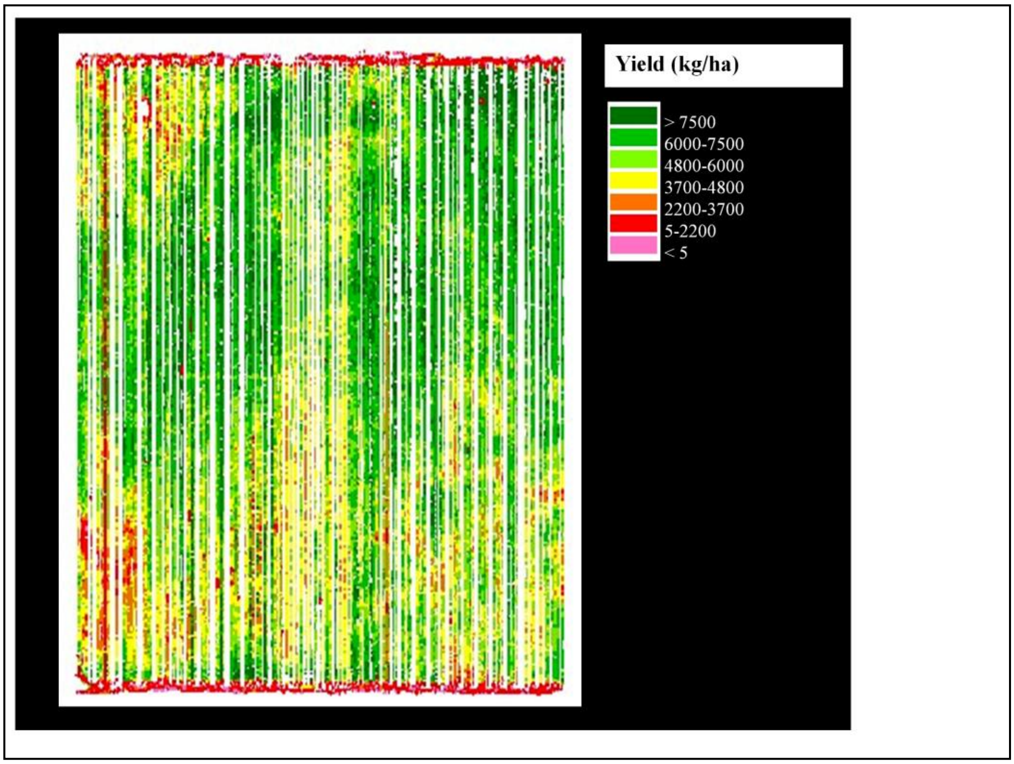

Image of the spatial yield data collected with the cotton yield monitor. Spatial distribution can be seen.

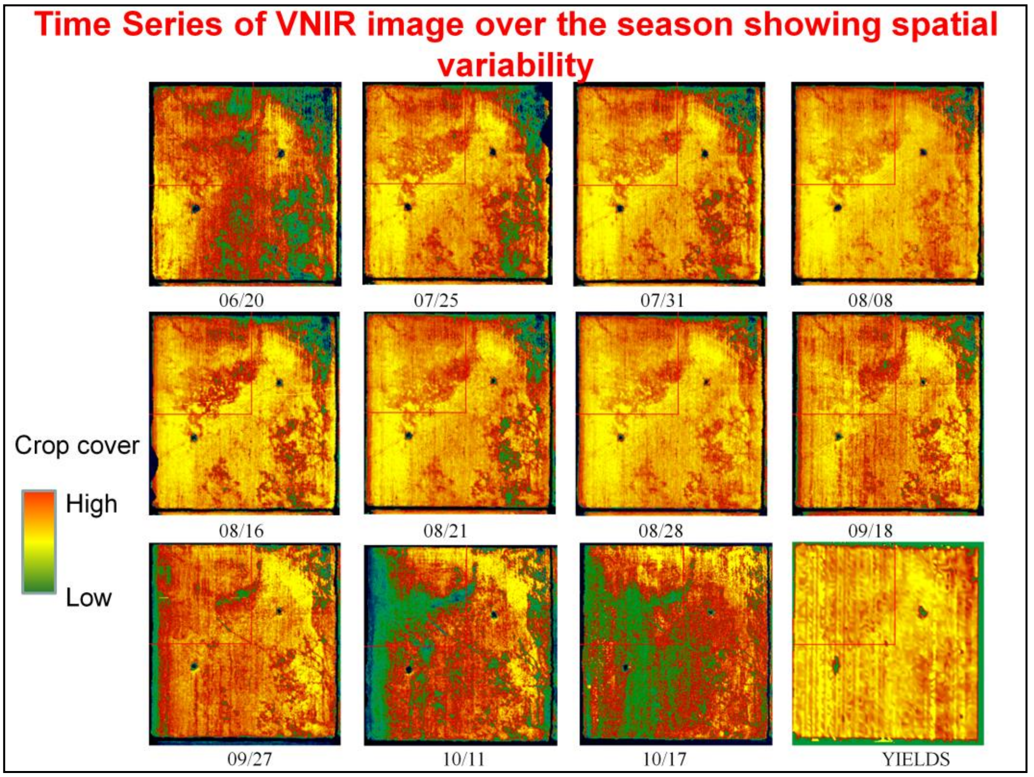

This is a color composite of the airborne hyperspectral imagery collected for each date. We can see how the cotton develops and the spatial changes over time.

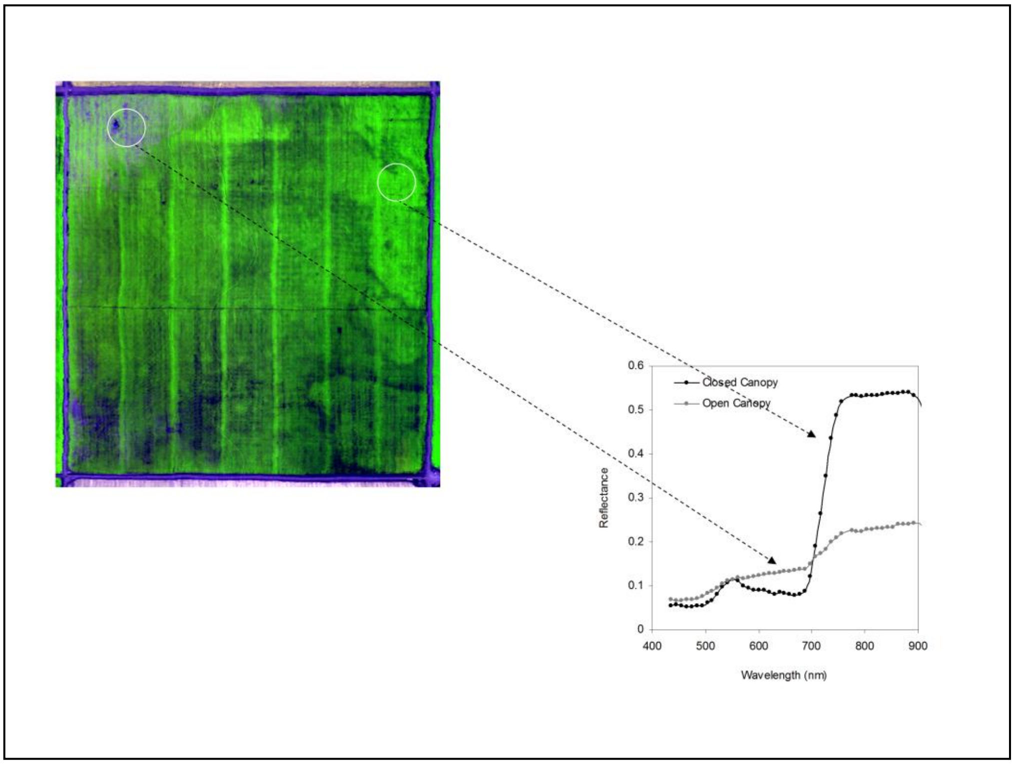

Hyperspectral data from the reflectance image at different areas of the field, for low and high growth. It shows good spectral shape.

1. Hyperspectral Indices Calculation

34 hyperspectral indices related to

⇒ crop cover and canopy structure (LAI, …)

⇒ chlorophyll *a*+*b*

⇒ canopy water content

⇒ red edge parameters

… calculated from the weekly hyperspectral reflectance images

- Indexes enabled comparison to spatial yield data and each index at each acquisition time
- Best indices for obtaining yield variability in cotton was assessed
- Time dependence of such specific indices with time

Calculation of indices from AVNIR hyperspectral data.

Growth differences due to site quality

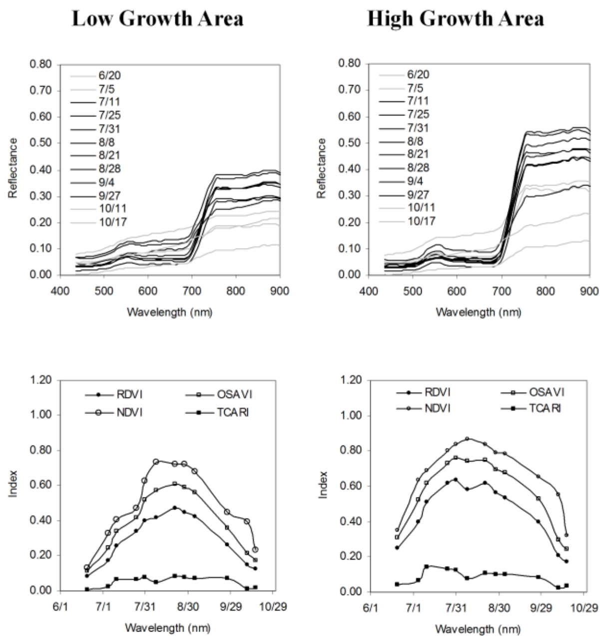

Time series of reflectance (up) and indices (bottom) for low (left) and high (right) growth areas show consistent spectra and indices calculated from the imagery. The time series show the behavior of indices over time as the crop develops.

Significant relationships between indices during summer and final yield

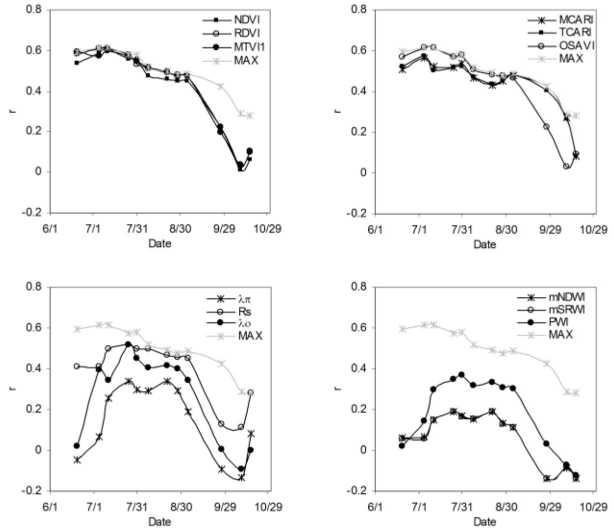

Relationships between yield and structural indcies (top left), chlorophyll (top right), red edge (lower left), and water indices (lower right). The MAX label indices the maximum relationship between yield and any index at any time. It shows that structural indices perform better at early stages, while chlorophyll indices perform better at later stages right before harvest.

2. Field Segmentation using Hyperspectral Indices

The indices were evaluated for detecting within-field areas of homogeneous yield

⇒ unsupervised *K-means* classifier applied to spatial yield data
⇒ to all hyperspectral indices

• Three classes were obtained using *K-means* clustering for areas of high, medium and low yield for
⇒ airborne imagery
⇒ spatial yield map

Field segmentation was performed to derive within-field areas of homogeneous yield into 3 clases= high yield, medium, and low yield areas.

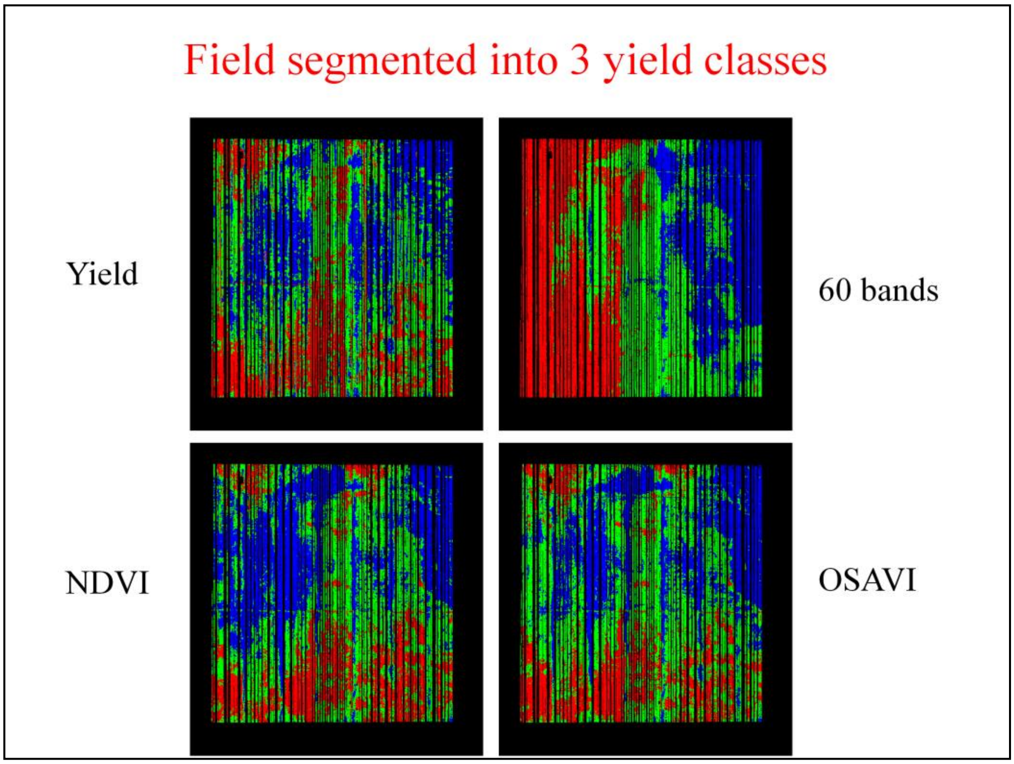

Yield classes obtained with k-means with 60 bands, NDVI and OSAVI a input, compared with 3 classes obtained from the yield image.

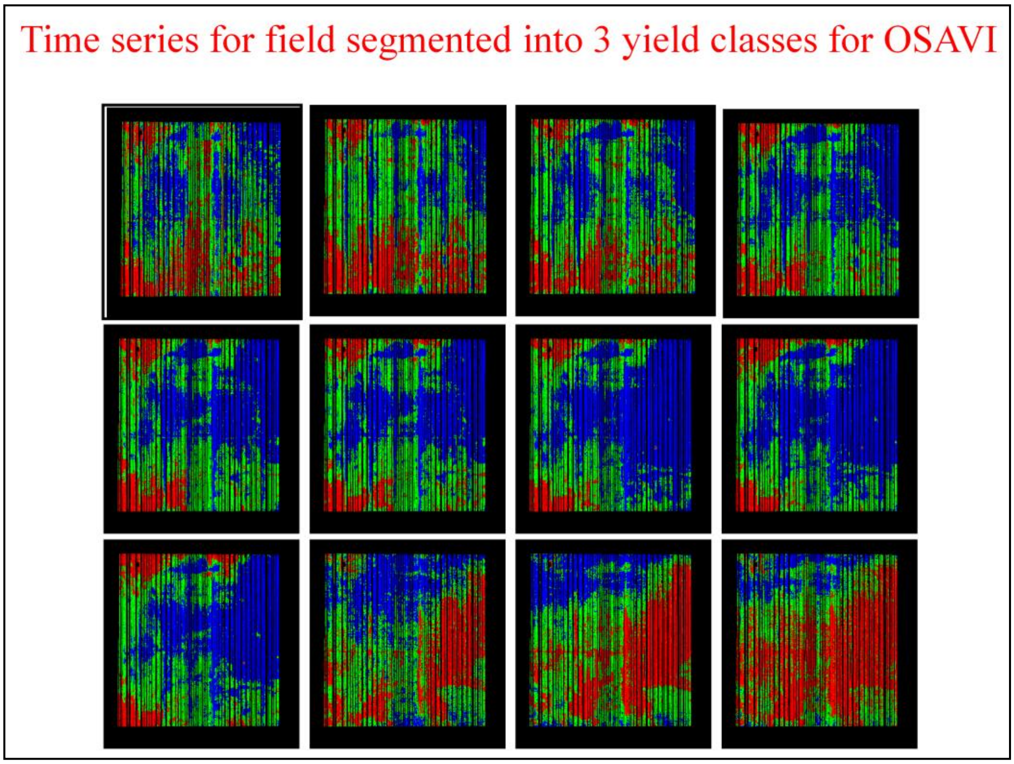

Time series of the field segmentation into three clases for OSAVI index. It can be seen that field segmentation accuracy is function of the time on the season. Classes size and distribution change over time.

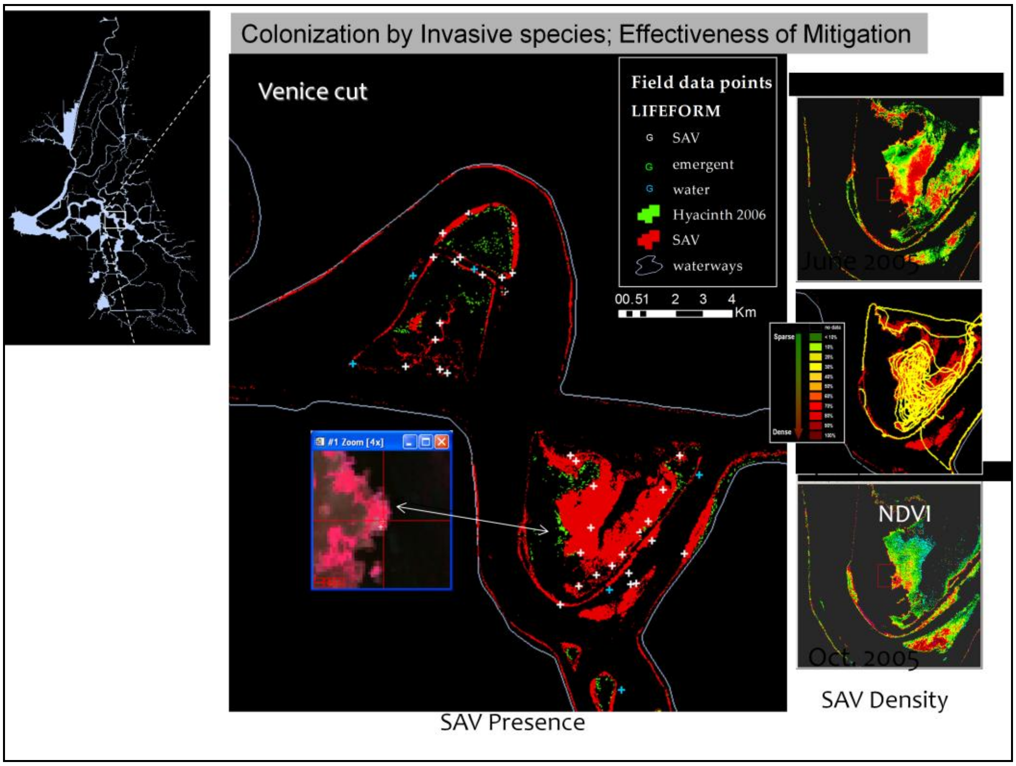
Colonization by Invasive species; Effectiveness of Mitigation
Venice cut
Field data points
LIFEFORM
SAV
emergent
water
Hyacinth 2006
SAV
waterways
00.51 2 3 4 Km
June 2005
NDVI
Oct. 2005
Sparse
Dense
SAV Presence
SAV Density

Is emergent vegetation expanding?

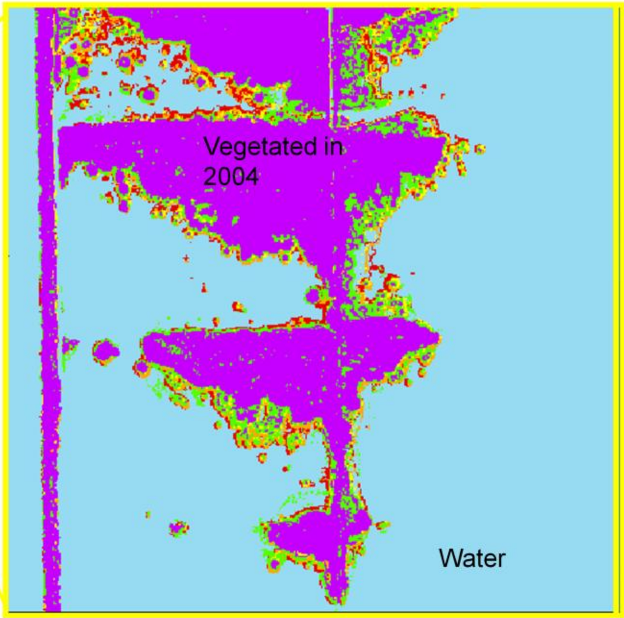

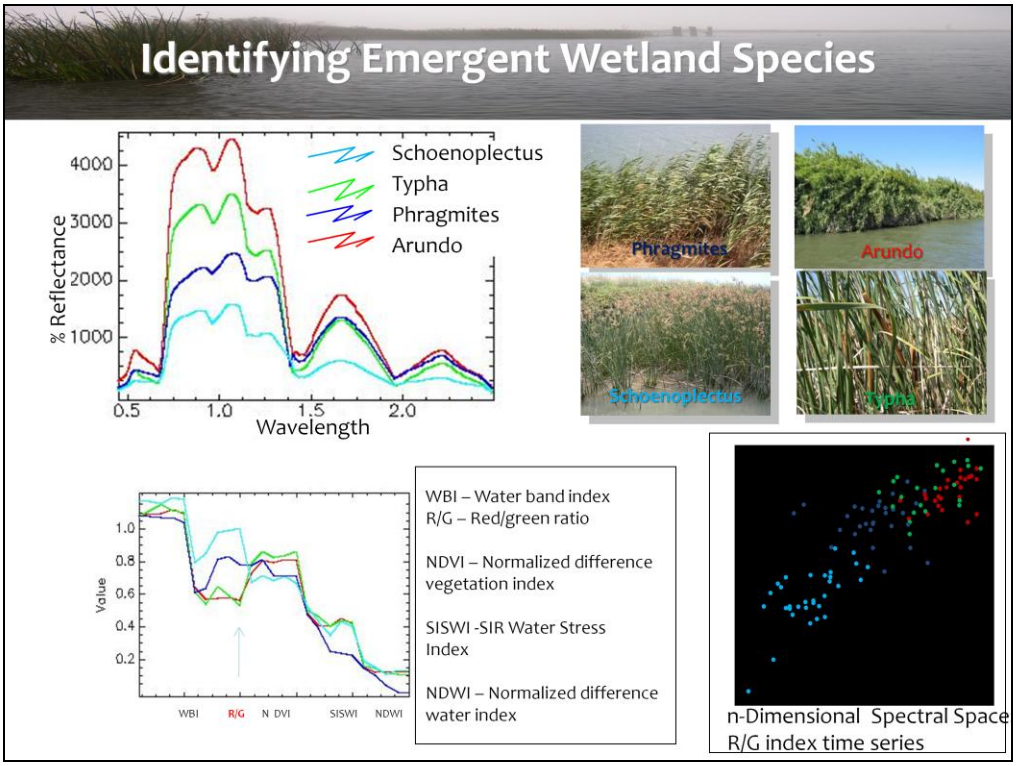

Red-green ratio usefull to distinguish the 4 species

Wetland Species and Other Plant Categories

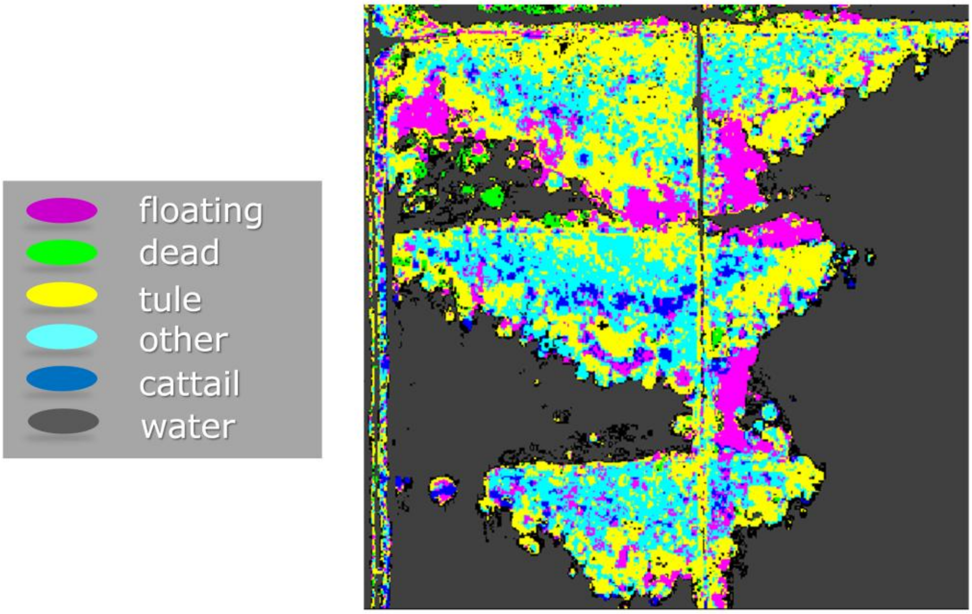

NASA Earth Observatory
Go to this web site to see their collection of time series examples

http://earthobservatory.nasa.gov/Features/WorldOfChange/

What You should know from this lecture:

1. Changes are due to (1) Biological changes with phenology, (2) seasonal and interannual changes by replacement
2. Changes due to physical conditions (sun-angles, clouds, aerosols, weather, precipitation
3. Land Use Change
4. Examples of monitoring change (what kinds of uses)
5. Some methods for data extraction